

ARMY RESEARCH LABORATORY



Dynamic Uniaxial Tensile Loading of Vector Polymers

by Johnathan Niemczura, Joe Lenhart, and Randy Mrozek

ARL-TR-5812

November 2011

NOTICES

Disclaimers

The findings in this report are not to be construed as an official Department of the Army position unless so designated by other authorized documents.

Citation of manufacturer's or trade names does not constitute an official endorsement or approval of the use thereof.

Destroy this report when it is no longer needed. Do not return it to the originator.

Army Research Laboratory

Aberdeen Proving Ground, MD 21005-5069

ARL-TR-5812

November 2011

Dynamic Uniaxial Tensile Loading of Vector Polymers

Johnathan Niemczura

Oak Ridge Institute for Science and Education

Joe Lenhart and Randy Mrozek

Weapons and Materials Research Directorate, ARL

REPORT DOCUMENTATION PAGE

Form Approved
OMB No. 0704-0188

Public reporting burden for this collection of information is estimated to average 1 hour per response, including the time for reviewing instructions, searching existing data sources, gathering and maintaining the data needed, and completing and reviewing the collection information. Send comments regarding this burden estimate or any other aspect of this collection of information, including suggestions for reducing the burden, to Department of Defense, Washington Headquarters Services, Directorate for Information Operations and Reports (0704-0188), 1215 Jefferson Davis Highway, Suite 1204, Arlington, VA 22202-4302. Respondents should be aware that notwithstanding any other provision of law, no person shall be subject to any penalty for failing to comply with a collection of information if it does not display a currently valid OMB control number.

PLEASE DO NOT RETURN YOUR FORM TO THE ABOVE ADDRESS.

1. REPORT DATE (DD-MM-YYYY) November 2011		2. REPORT TYPE Final		3. DATES COVERED (From - To) March 2010–March 2011	
4. TITLE AND SUBTITLE Dynamic Uniaxial Tensile Loading of Vector Polymers				5a. CONTRACT NUMBER	
				5b. GRANT NUMBER	
				5c. PROGRAM ELEMENT NUMBER	
6. AUTHOR(S) Johnathan Niemczura, * Joe Lenhart, and Randy Mrozek				5d. PROJECT NUMBER AH80	
				5e. TASK NUMBER	
				5f. WORK UNIT NUMBER	
7. PERFORMING ORGANIZATION NAME(S) AND ADDRESS(ES) U.S. Army Research Laboratory ATTN: RDRL-WMP-B Aberdeen Proving Ground, MD 21005-5069				8. PERFORMING ORGANIZATION REPORT NUMBER ARL-TR-5812	
9. SPONSORING/MONITORING AGENCY NAME(S) AND ADDRESS(ES)				10. SPONSOR/MONITOR'S ACRONYM(S)	
				11. SPONSOR/MONITOR'S REPORT NUMBER(S)	
12. DISTRIBUTION/AVAILABILITY STATEMENT Approved for public release; distribution unlimited.					
13. SUPPLEMENTARY NOTES * Oak Ridge Institute for Science and Education, 4692 Millennium Drive, Ste. 101, Belcamp, MD 21017					
14. ABSTRACT During this analysis, we investigated tensile wave propagation using a strip stretcher with the goal of finding constitutive properties for soft materials of interest to the U.S. Army Research Laboratory. We found the power-law model to be adequate for matching small strain response prior to reflection for the polymers not undergoing localization. After examining the Swanson model, we found that it matched the power-law response.					
15. SUBJECT TERMS polymers, dynamic tension, wave propagation, Swanson model					
16. SECURITY CLASSIFICATION OF:			17. LIMITATION OF ABSTRACT	18. NUMBER OF PAGES	19a. NAME OF RESPONSIBLE PERSON
a. REPORT	b. ABSTRACT	c. THIS PAGE			19b. TELEPHONE NUMBER (Include area code)
Unclassified	Unclassified	Unclassified	UU	66	Michael Scheidler (410) 278-5436

Contents

List of Figures	v
List of Tables	vii
Acknowledgments	viii
1. Introduction	1
2. Experimental Setup	1
3. One-Dimensional Analysis: Closed Form Solution With Power-Law Model	2
4. One-Dimensional Analysis: Riemann Invariants	3
5. Three-Dimensional Analysis With Swanson Model	5
6. Mesh and Boundary Conditions	6
7. Analysis of Experiments	7
8. Vector 4111 Specimens	10
8.1 Test 4111o1	10
8.2 Test 4111o2	14
9. Vector 4211 Specimens	18
9.1 Test 4211o1	19
9.2 Test 4211o2	23
9.3 Test 4211o3	26
9.4 Test 4211o4	29
10. Vector 4411 Specimens	33
10.1 Test 4411o1	34
10.2 Test 4411o2	37
10.3 Test 4411o3	41

10.4 Test 4411o4	43
11. Cross-Section Analysis of 4211o2	45
12. Conclusions	47
13. References	49
Distribution List	50

List of Figures

Figure 1. Experimental setup.	2
Figure 2. Nominal stress-strain relation for tests 4111o1 and 4111o2.	10
Figure 3. y-t diagram for test 4111o1.	11
Figure 4. Nominal stress-strain relation for test 4111o1.	12
Figure 5. Strain-rate as a function of time for test 4111o1.	12
Figure 6. Numerical simulations with experimental results for test 4111o1.	13
Figure 7. True stress as a function of log strain for test 4111o1.	13
Figure 8. Time history of true stress from numerical simulations for test 4111o1.	14
Figure 9. y-t diagram for test 4111o2.	15
Figure 10. Nominal stress-strain relation for test 4111o2.	15
Figure 11. Strain rate as a function of time for test 4111o2.	16
Figure 12. Numerical simulations with experimental results for test 4111o2.	17
Figure 13. True stress as a function of log strain for test 4111o2.	17
Figure 14. Time history of true stress from numerical simulations for test 4111o2.	18
Figure 15. Nominal stress-strain relation for vector 4211 specimens.	18
Figure 16. y-t diagram for test 4211o1.	19
Figure 17. Nominal stress-strain relation for test 4211o1.	19
Figure 18. Strain rate for test 4211o1.	20
Figure 19. Numerical simulations with experimental results for test 4211o1.	21
Figure 20. True stress as a function of log strain for test 4211o1.	22
Figure 21. Time history of true stress from numerical simulations for test 4211o1.	22
Figure 22. y-t diagram for test 4211o2.	23
Figure 23. Nominal stress-strain relation for test 4211o2.	23
Figure 24. Strain rate as a function of time for test 4211o2.	24
Figure 25. Numerical simulations with experimental results for test 4211o2.	25
Figure 26. True stress as a function of log strain for test 4211o2.	25
Figure 27. Time history of true stress from numerical simulations for test 4211o2.	26
Figure 28. y-t diagram for test 4211o3.	26
Figure 29. Nominal stress-strain relation for test 4211o3.	27
Figure 30. Strain rate as a function of time for test 4211o3.	27
Figure 31. Numerical simulations with experimental results for test 4211o3.	28

Figure 32. True stress as a function of log strain for test 4211o3.....	29
Figure 33. Time history of true stress from numerical simulations for test 4211o3.....	29
Figure 34. y-t diagram for test 4211o4.	30
Figure 35. Nominal stress-strain relation for test 4211o4.....	30
Figure 36. Strain rate as a function of time for test 4211o4.	31
Figure 37. Numerical simulations with experimental results for test 4211o4.	32
Figure 38. True stress as a function of log strain for test 4211o4.....	32
Figure 39. Time history of true stress from numerical simulations for test 4211o4.....	33
Figure 40. Summary of stress-strain relations for tests 4411o1 and 4411o2.....	34
Figure 41. y-t diagram for test 4411o1.	34
Figure 42. Nominal stress-strain relation for test 4411o1.....	35
Figure 43. Strain rate as function of time for test 4411o1.	35
Figure 44. Numerical simulations with experimental results for test 4411o1.	36
Figure 45. True stress as a function of log strain for test 4411o1.....	37
Figure 46. Time history of true stress from numerical simulations for test 4411o1.....	37
Figure 47. y-t diagram for test 4411o2.	38
Figure 48. Nominal stress-strain relation for test 4411o2.....	38
Figure 49. Strain rate as a function of time for test 4411o2.	39
Figure 50. Numerical simulations with experimental results for test 4411o2.	40
Figure 51. True stress as a function of log strain for test 4411o2.....	40
Figure 52. Time history of true stress from numerical simulations for test 4411o2.....	41
Figure 53. y-t diagram for test 4411o3.	42
Figure 54. Nominal stress-strain relation for test 4411o3.....	42
Figure 55. Strain rate as a function of time for test 4411o3.	43
Figure 56. y-t diagram for test 4411o4.	43
Figure 57. Nominal stress-strain relation for test 4411o4.....	44
Figure 58. Strain rate as a function of time for test 4411o4.	44
Figure 59. True stress along axis through half-width.	45
Figure 60. True stress along axis through half-thickness.	46
Figure 61. Log strain along axis through half-width.	46
Figure 62. Log strain along axis through half-thickness.....	47

List of Tables

Table 1. Parameters for power-law model.....	8
Table 2. Swanson parameters for tests.....	9

Acknowledgments

We would like to thank the following individuals:

- Mike Scheidler and Stephan Bilyk for their help in bringing everything together that we needed to perform this work.
- Bryan Love for his tutelage in using Presto.
- Dave MacKenzie and Bill Edmanson for the tremendous job they did designing and assembling the experimental equipment and operating the air gun used in EF 167; it was a pleasure working with them.
- Seth Halsey for his services in setting up and operating the high-speed camera during the experiments.

This research was supported in part by an appointment to the Postgraduate Research Participation Program at the U.S. Army Research Laboratory (ARL) administered by the Oak Ridge Institute for Science and Education through an interagency agreement between the U.S. Department of Energy and ARL.

1. Introduction

In this report, we examine the propagation of tensile waves of finite deformation in long, thin strips of soft elastomers. The results of experiments, analysis, and numerical simulations are used to determine fits to several nonlinear elastic constitutive models. These model calibrations represent the dynamic tensile response of the elastomers. Quasi-static tensile stress-strain data is included for comparison.

The elastomers used in this study were styrene-isoprene-styrene block copolymers of varying stiffness. The high-rate tensile wave propagation experiments were conducted by holding one end of the specimen fixed and displacing the other end at constant velocity by means of a projectile fired from a gas gun. A high-speed video camera was used to monitor the position of markers on the specimens. The various elastic constitutive models are calibrated to match this particle trajectory data.

Two classes of models were considered here: a simple one-dimensional (1-D) power-law model for the stress-strain curve and a fully three-dimensional (3-D) nonlinear elastic constitutive model.

2. Experimental Setup

Figure 1 shows the experimental setup. A strip of rubber is wrapped around the muzzle of an air gun. A polycarbonate flange, inserted into the muzzle, is used to apply the loading velocity to the strip at $x = 0$ after impact by a steel slug projectile. The flange has two sets of grooves. One set, denoted as the specimen channel, keeps the specimen from displacing in the lateral direction. The other set allows air to vent from the gun as the projectile travels down the barrel. The strip is clamped to the outside of the barrel at $x = L$. A Photron SA1 high-speed video camera with a framing rate of 200,000 frames/s was used to record the movement of marker lines drawn on the specimen as a function of time. The dashed line along the length of the specimen denotes the row of pixels for each image that was used in creating a y-t diagram.

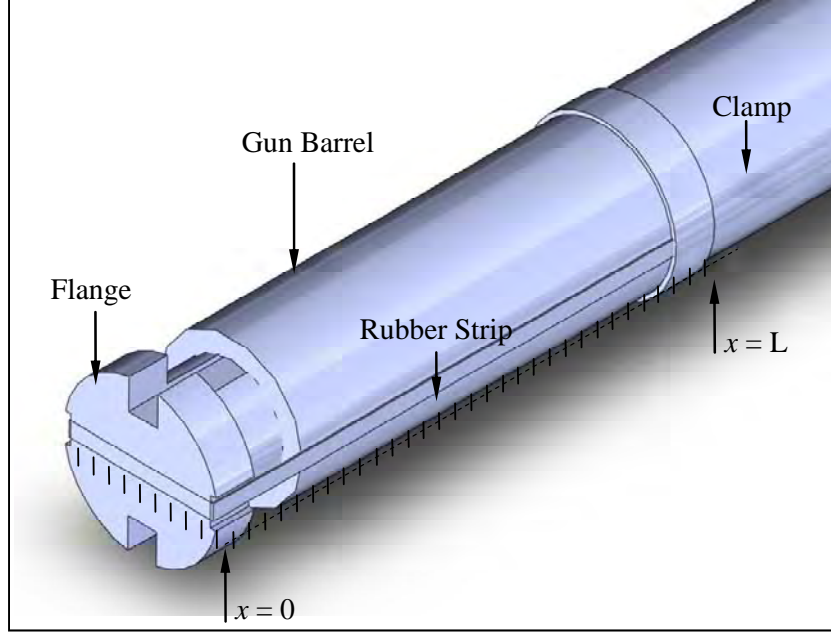


Figure 1. Experimental setup.

3. One-Dimensional Analysis: Closed Form Solution With Power-Law Model

The 1-D analysis follows the steps described in Niemczura and Ravi-Chandar (2011a). We have a strip of material whose length is much greater than the width and thickness. As a result, we first consider the specimen to be semi-infinite with material occupying the space $0 \leq x < \infty$, where x is a position in the reference configuration, and we ignore lateral inertia terms associated with lateral motion. Only one boundary condition is prescribed with a constant velocity $-V$ at $x = 0$ for $t > 0$. This boundary condition produces tensile wave propagation in the positive x direction displacing the particles to the current position $y(x, t) = x + u(x, t)$. The strain and particle velocity are given by $\gamma(x, t) = \partial u / \partial x = \gamma(\xi)$ and $v(x, t) = \partial u / \partial t = v(\xi)$, respectively. The last term in the definitions of strain and particle velocity result from the lack of length scales and time scales, thereby producing a dependence on only $\xi = x/t$. The governing equations of motion for this 1-D wave problem in a nonlinearly elastic material are

$$\begin{aligned} \frac{\partial \sigma}{\partial x} &= \rho \frac{\partial v}{\partial t} \\ \frac{\partial v}{\partial x} &= \frac{\partial \gamma}{\partial t} \end{aligned}, \quad (1)$$

where ρ is the mass density per unit volume (constant) and σ is the nominal stress. Equation 1 is expressed in terms of particle displacement to obtain the wave equation

$$[c(\gamma)]^2 \frac{\partial^2 u}{\partial x^2} = \frac{\partial^2 u}{\partial t^2}, \quad (2)$$

where $c(\gamma) = \sqrt{\sigma'(\gamma)/\rho}$ is the wave speed in the reference configuration and can be a nonlinear function of strain. Prime denotes a derivative with respect to the argument.

For the stress-strain relation in the 1-D analysis, a power-law model is assumed:

$$\sigma = \sigma_0 + \mu(\gamma - \gamma_0)^n, \quad (3)$$

where σ_0 is the stress at the initial strain γ_0 , μ is the reference stress, and n is the ‘‘hardening’’ parameter; in order to generate simple waves, the only restriction required in this model is that $0 < n < 1$. The allowance for an initial strain in the model results from analysis conducted by Niemczura and Ravi-Chandar (2011a, 2011b). An initial stiff response was followed by softening regardless of initial strain. σ_0 corresponds to loading from a quasi-static state. In this report, the initial strain is practically zero.

With this model, wave speed as a function of strain is

$$c(\gamma) = \left(\frac{n\mu}{\rho} \right)^{1/2} (\gamma - \gamma_0)^{\frac{n-1}{2}}. \quad (4)$$

Note that as $\gamma \rightarrow \gamma_0$, $c \rightarrow \infty$; there is no limit to the wave speed at small strains. While this may pose no problem for a closed-form solution, a finite wave speed may be needed in numerical simulations. We can rearrange equation 4 to obtain strain as a function of ξ :

$$\gamma = \gamma_0 + \left(\frac{n\mu}{\rho} \right)^{\frac{1}{1-n}} \xi^{\frac{2}{n-1}}. \quad (5)$$

The particle displacement is obtained by integrating equation 5 with respect to x with t held fixed:

$$u(x, t) = \gamma_0 x + \frac{n-1}{n+1} \left(\frac{n\mu}{\rho} \right)^{\frac{1}{1-n}} x^{\frac{n+1}{n-1}} t^{\frac{2}{n-1}}. \quad (6)$$

4. One-Dimensional Analysis: Riemann Invariants

For problems involving finite-length specimens, the similarity solution breaks down and one must resort to other methods of solutions. The method of characteristics is used for solving such problems. For the hyperbolic system in equation 1, the Riemann invariants are

$$\begin{aligned}
r^{(1)} &= \rho c v + \sigma \quad \text{on} \quad \frac{dx}{dt} = -c \\
r^{(2)} &= -\rho c v + \sigma \quad \text{on} \quad \frac{dx}{dt} = c
\end{aligned} \tag{7}$$

For this problem, the Riemann invariants, $r^{(k)}$, are constant along the characteristics, $\mp c$. In implementing this method, we divide the x -axis into discrete nodes and time into a series of time steps. Let x_i^k denote the node at i during time-step k . The time increment at each step is calculated such that the fastest wave speed from the previous time step satisfies the Courant-Friedrichs-Levy condition. In addition, x_-^k is the origin of the characteristic, $-c_-^k$, that arrives at x_i^{k+1} and is located between nodes x_i^k and x_{i+1}^k ; similarly, x_+^k is the origin of the characteristic, $+c_+^k$, that arrives at x_i^{k+1} and is located between nodes x_{i-1}^k and x_i^k . We then require

$$\begin{aligned}
r^{(1)}(x_i^{k+1}) &= r^{(1)}(x_-^k) \\
r^{(2)}(x_i^{k+1}) &= r^{(2)}(x_+^k)
\end{aligned} \tag{8}$$

Given the state at time step k , $[v(x^k), \sigma(x^k)]$, we can use the above algorithm to march in time; we obtain $\sigma(x_i^{k+1})$ first:

$$\sigma(x_i^{k+1}) = \frac{\rho}{2} (c_-^k v(x_-^k) - c_+^k v(x_+^k)) + \frac{1}{2} (\sigma(x_-^k) + \sigma(x_+^k)). \tag{9}$$

Then, c_i^{k+1} is calculated using $\sigma(x_i^{k+1})$ since we assume that the constitutive law is known. Next, the particle velocity is calculated,

$$v(x_i^{k+1}) = \frac{1}{2c_i^{k+1}} (c_-^k v(x_-^k) + c_+^k v(x_+^k)) + \frac{1}{2\rho c_i^{k+1}} (\sigma(x_-^k) - \sigma(x_+^k)). \tag{10}$$

It is clear that appropriate boundary conditions must be prescribed; the simplest cases are when either the particle velocity or the stress is prescribed at the boundary. It is also possible to prescribe more complicated relationships with some relation between the stress and particle velocity or displacement to simulate compliant boundaries or interfaces. The particle trajectory is then calculated as $y(x_i^{k+1}) = x_i^k + v(x_i^{k+1}) dt$ with dt equal to the time step between $k+1$ and k . With this procedure, we can deal with prescribed boundary conditions on either end of a finite rubber strip. Therefore, given an appropriate constitutive relation, the method of characteristics can be used to determine the response of a finite-length specimen.

5. Three-Dimensional Analysis With Swanson Model

Presto, a Lagrangian hydrocode, simulates the experiments accounting for the finite width and thickness (SIERRA Solid Mechanics Team, 2010). A Swanson hyperelastic material (Swanson, 1985) is used with the strain energy function:

$$U = \frac{1.5A_1(I_1/3-1)^{(P_1+1)}}{(P_1+1)} + \frac{1.5B_1(I_2/3-1)^{(Q_1+1)}}{(Q_1+1)} + \frac{1.5C_1(I_1/3-1)^{(R_1+1)}}{(R_1+1)} + \frac{(J_m-1)^2}{D}. \quad (11)$$

The strain invariants I_1 and I_2 are the first two principal invariants of the right Cauchy-Green deformation tensor $F_m^T F_m$, where F_m is the mechanical deformation gradient. J_m is the mechanical Jacobian determinant, $J_m = \det[F_m]$.

The material constants A_1 , B_1 , and C_1 must be positive or zero. The material constant $D = 2/K$, where $K > 0$ is the bulk modulus; thus the last term on the right in equation 11 is always present. By the number of terms in the Swanson model, we mean the number of nonzero terms out of the first three terms on the right in equation 11. A one-term Swanson model has $A_1 > 0$ and $B_1 = C_1 = 0$; this model does not involve the invariant I_2 . A two-term Swanson model has $A_1 > 0$, $B_1 > 0$, and $C_1 = 0$; this model involves single I_1 and I_2 terms. The material constants P_1 and Q_1 in these first two terms should be negative or zero to match the small strain response. A three-term Swanson model has A_1 , B_1 , and C_1 positive and so has two I_1 terms; the material constant R_1 in the third term should be positive and used to match the large strain response.

If we assume incompressibility, then $J_m = \lambda_1 \lambda_2 \lambda_3 = 1$, and the first two strain invariants may be written as

$$\begin{aligned} I_1 &= \lambda_1^2 + \lambda_2^2 + \frac{1}{\lambda_1^2 \lambda_2^2}, \\ I_2 &= \frac{1}{\lambda_1^2} + \frac{1}{\lambda_2^2} + \lambda_1^2 \lambda_2^2, \end{aligned} \quad (12)$$

where λ_1 , λ_2 , and λ_3 are the principal stretches. For uniaxial loading, we have $\lambda_1 = \lambda$ along the principal axis of loading and $\lambda_2 = \lambda_3 = 1/\sqrt{\lambda}$ in the transverse directions. Equation 12 can now be rewritten as

$$\begin{aligned} I_1 &= \lambda^2 + \frac{2}{\lambda}, \\ I_2 &= \frac{1}{\lambda^2} + 2\lambda. \end{aligned} \quad (13)$$

The true stress-stretch relation for uniaxial loading is

$$\tau = \left(\lambda^2 - \frac{1}{\lambda} \right) \left[A_1 \left(\frac{I_1}{3} - 1 \right)^{P_1} + C_1 \left(\frac{I_1}{3} - 1 \right)^{R_1} + \frac{B_1}{\lambda} \left(\frac{I_2}{3} - 1 \right)^{Q_1} \right]. \quad (14)$$

True stress τ is defined with respect to nominal stress σ as $\tau = \lambda\sigma$ for the uniaxial case. For the uniaxial loading conditions, if we prescribe C_1 , P_1 , and Q_1 to be zero, then we arrive at the Mooney-Rivlin model

$$U = c_1(I_1 - 3) + c_2(I_2 - 3), \quad (15)$$

where $c_1 = A_1/2$ and $c_2 = B_1/2$. Please note for matching experimental results, we must not rely completely on one type of test to determine material parameters. Shear and compression response must be matched as well.

In the the Presto simulation, we must specify the Poisson's ratio, ν , and the bulk modulus, K . For the Swanson model, we prescribe the bulk modulus at a cutoff strain as

$$K = \frac{2 \left(A_1 \left(\frac{\varepsilon_{cut}^2}{3} \right)^{P_1} + B_1 \left(\frac{\varepsilon_{cut}^2}{3} \right)^{Q_1} \right) (1 + \nu)}{3(1 - 2\nu)}. \quad (16)$$

$\varepsilon_{cut} = 1$ and $\nu = 0.49999$ were used for all simulations. This cutoff strain ensures that a finite bulk modulus is supplied to the numerical simulation. An $\varepsilon_{cut} = 0$ or $\nu = 0.5$ would cause an infinite bulk modulus. The bulk modulus affects the wave speeds, and thereby the time steps, in the numerical simulation.

6. Mesh and Boundary Conditions

We performed numerical simulations with Presto using only one-quarter of the cross section of the specimen strip to reduce the computational time. The specimen length was preserved, but only half the width and thickness was examined. The newly created faces were prescribed zero perpendicular displacement so that the deformation of the quartered specimen would be the same as that of a full specimen. The dimension of the specimen in the simulations is then 0.0025 m for the half width, 0.3 m for the length, and 0.00025 m for the half thickness. Twenty elements span the half width of the specimen, and two elements span the half thickness. The loading end of the specimen at $x = 0$ m was prescribed a loading velocity measured from the experiment, and the other end at $x = 0.3$ m was prescribed a silent boundary condition to minimize reflection. This silent boundary can minimize reflection of low- to medium-frequency waves but may still allow significant reflection of high-frequency waves. The length of the specimen is longer than the length of the actual experimental specimen to minimize reflection. While the experiments suggest the specimen experiences an instantaneous jump in velocity, a small ramp up to the final

loading velocity is provided over $4e-5$ s in the Presto simulations. This small ramp eliminates the creation of high-frequency waves that contribute to hour-glassing of elements near the impact end. Without the ramp, the hour-glassed elements distort severely, leading to inverted elements and a discontinuation of the simulation before the loading waves have traveled any significant distance into the specimen.

7. Analysis of Experiments

A series of steps is taken when analyzing the experiments. First, we create a y-t diagram from the high-speed images. In all y-t diagrams, the horizontal resolution is 6401 pixels/m and the vertical resolution is 200,000 pixels/s. The y-t diagram is cut so that the impact point at the time of impact is at the lower-left side of the figure. Using the horizontal resolution, we write the position of each line in the y-t diagram in terms of the material reference frame position. A closed-form solution using a power-law model is then matched to the experimental trajectories by adjusting the parameters n and μ . Next, we measure the loading velocity from the y-t diagram; using this velocity and power-law parameters, we compare a Riemann simulation to the y-t diagram to confirm the measured loading velocity. At this point, the power-law model is extended to large strains and plotted as a true stress-strain curve. The parameters in the Swanson model are then adjusted to match the power-law true stress-strain curve for this uniaxial case; this is a visual match, not an optimization procedure. Optimization should be implemented once compression and/or shear tests add additional restrictions to the matching process. A numerical simulation using Presto is then implemented with a set of parameters in the Swanson model for each test of interest. Three different sets of parameters are compared to each test.

The materials tested are polymers and consist of styrene-isoprene-styrene block copolymer manufactured by Dexco Polymers; the specimens were prepared at ARL. Three batches of the block material were made with each batch containing a different amount of styrene. The styrene portions of the block are stiff when compared to the rubbery isoprene. The styrene portion acts as cross-links in the material. The first batch is vector 4111 and is the softest of the batch materials. The second batch is vector 4211, and the third batch is vector 4411. Vector 4411 has the stiffest response of the three batches. While vectors 4111 and 4211 have elastic responses to large strains, vector 4411 has an instability in its stress-strain relation where a localization leads to a permanent deformation. Four tests were conducted for each batch of material with one specimen used in each test (i.e., no strip of polymer was stretched twice). The batch test identifier is denoted by “vector4X11oY”, where “X” signifies the batch group and “Y” denotes the actual test number.

For each test, table 1 lists the parameters in the power-law model that gave the best fit to the experimental trajectories. Also included in this table are the specimen density ρ , the loading velocity V , the initial strain γ_0 in the specimen, and the strain γ_{end} at the end of the 1-D analysis.

Table 1. Parameters for power-law model.

Test	μ (MPa)	n	γ_0	γ_{end}	ρ (kg/m ³)	V (m/s)
Test 4111o1	1.1	0.55	0.022	0.28	926	11.3
Test 4111o2	1.1	0.55	0.031	0.32	926	12.2
Test 4111o3	1.5	0.4	0.044	1.54	926	18.877
Test 4211o1	1.2	0.3	0.036	0.087	940	4.2
Test 4211o2	1.4	0.4	0.058	0.27	940	11.89
Test 4211o3	2.4	0.33	0.094	0.419	940	23.8
Test 4211o4	3.5	0.27	0.018	0.451	940	31.25
Test 4411o1	50	0.45	0	0.0278	968	15.62
Test 4411o2	55	0.45	0.018	0.056	968	20.83
Test 4411o3	55	0.4	0.009	0.031	968	14.84
Test 4411o4	30	0.43	0.019	0.053	968	14.51

Table 2 lists the parameters in the Swanson model that gave the best match to the power-law true stress-strain curve. For each test, the parameters for one-, two-, and three-term Swanson models were obtained.

Table 2. Swanson parameters for tests.

Test	A_1 (MPa)	P_1	B_1 (MPa)	Q_1	C_1 (MPa)	R_1	$K(\epsilon_{cut} = 1)$ (GPa)
Test 4111o1 1-term Swanson	0.525	-0.16	0	0	0	0	31.3
Test 4111o1 2-term Swanson	0.22	-0.2	0.4	-0.1	0	0	36.0
Test 4111o1 3-term Swanson	0.2	-0.2	0.4	-0.1	0.2	0.2	34.8
Test 4111o2 1-term Swanson	0.525	-0.16	0	0	0	0	31.3
Test 4111o2 2-term Swanson	0.22	-0.2	0.4	-0.1	0	0	36.0
Test 4111o2 3-term Swanson	0.2	-0.2	0.4	-0.1	0.2	0.2	34.8
Test 4211o1 1-term Swanson	0.5	-0.32	0	0	0	0	35.5
Test 4211o1 2-term Swanson	0.2	-0.36	0.55	-0.17	0	0	48.0
Test 4211o1 3-term Swanson	0.19	-0.36	0.55	-0.17	0.19	0.36	47.3
Test 4211o2 1-term Swanson	0.55	-0.28	0	0	0	0	37.4
Test 4211o2 2-term Swanson	0.2	-0.36	0.55	-0.15	0	0	47.3
Test 4211o2 3-term Swanson	0.22	-0.36	0.55	-0.15	0.22	0.36	48.8
Test 4211o3 1-term Swanson	1.25	-0.28	0	0	0	0	85.0
Test 4211o3 2-term Swanson	0.6	-0.33	1	-0.15	0	0	102.1
Test 4211o3 3-term Swanson	0.58	-0.33	1	-0.15	0.58	0.33	100.6
Test 4211o4 1-term Swanson	1.5	-0.33	0	0	0	0	107.8
Test 4211o4 2-term Swanson	0.7	-0.4	1.6	-0.1	0	0	143.6
Test 4211o4 3-term Swanson	0.6	-0.4	1.6	-0.1	0.6	0.4	135.8
Test 4411o1 1-term Swanson	17.5	-0.27	0	0	0	0	1177.1
Test 4411o1 2-term Swanson	10.5	-0.3	5	-0.25	0	0	1059.0
Test 4411o1 3-term Swanson	12	-0.3	5	-0.25	12	0.3	1163.2
Test 4411o2 1-term Swanson	19.5	-0.27	0	0	0	0	1311.7
Test 4411o2 2-term Swanson	15.5	-0.27	4.8	-0.25	0	0	1358.5
Test 4411o2 3-term Swanson	15	-0.27	4.8	-0.25	15	0.27	1324.8

8. Vector 4111 Specimens

Vector 4111 specimens are the softest of the three batches. Four tests were conducted, but only the first two are shown in this report. Tests 4111o3 and 4111o4 cannot be used since specimen motion exists prior to impact. Figure 2 shows a summary of the nominal stress-strain relation for these two tests using the power-law model. Given that the impact velocity and initial strain are almost identical, the stress-strain relations are almost identical.

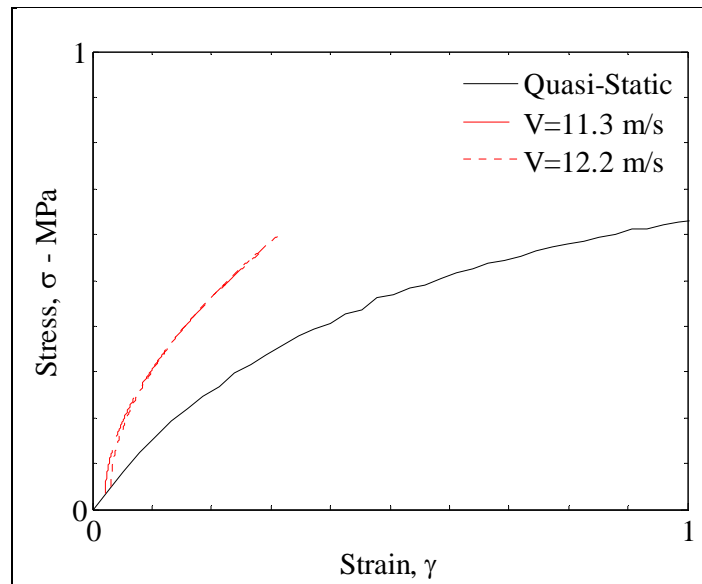


Figure 2. Nominal stress-strain relation for tests 4111o1 and 4111o2.

8.1 Test 4111o1

Figure 3 shows the y - t diagram for test 4111o1. The loading velocity (the velocity of the flange) is 11.3 m/s from the y - t diagram. On top of the y - t diagram are red dashed lines showing particle trajectories obtained from a 1-D analysis using the parameters $n = 0.55$ and $\mu = 1.1$ MPa for the power-law model. The initial strain was $\gamma_0 = 0.022$. The strain at the end of the 1-D analysis was $\gamma_{end} = 0.28$. The largest strain in the y - t diagram was $\gamma_{max} = 2.62$.

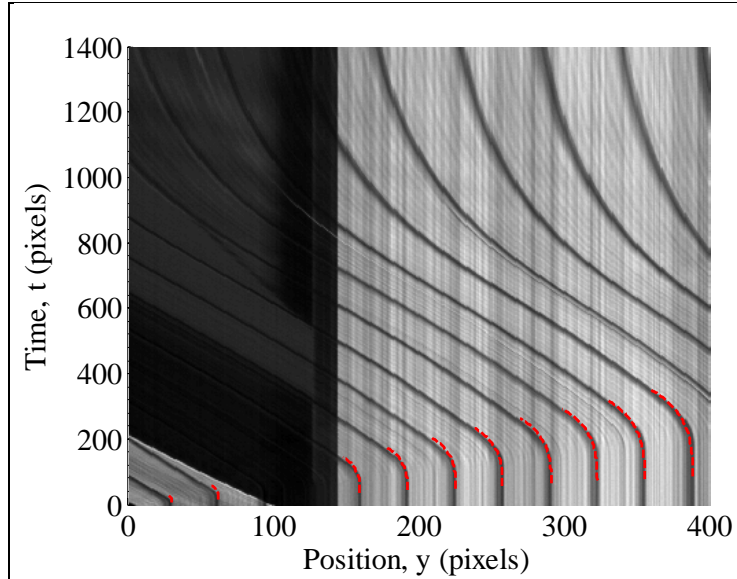


Figure 3. y-t diagram for test 4111o1.

Note that the specimens are transparent. Black indelible ink is used to mark positions of interest. In order to contrast these lines against the normally dark background, beige masking tape was attached to part of the flange and gun barrel. This tape is a simple way to lighten the background. As the flange moves away from the barrel, the image becomes dark since the tape is attached to the flange. Initially, there is a gap between the end of the specimen channel and the front of the barrel; this gap grows with time after impact and is a result of the plug portion of the flange partial insertion in the gun barrel. No tape is used on the plug portion since tolerances between the plug and gun barrel are specified for a tight fit with no room to slide tape between the barrel and plug.

The change in particle trajectories beyond the power-law model match is the result of reflection from the fixed boundary. This change results in a decrease in particle velocity and a further increase of strain.

Figure 4 shows the stress-strain relation for test 4111o1 using the power-law model. This dynamic stress-strain relation is a little stiffer than the quasi-static case.

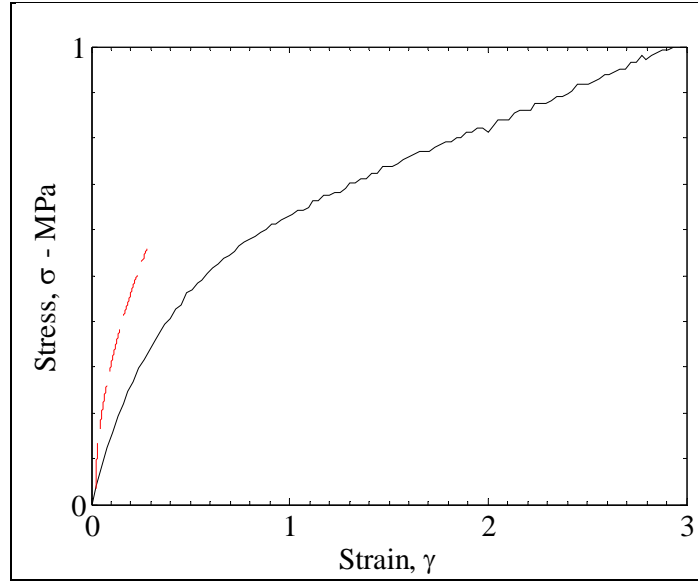


Figure 4. Nominal stress-strain relation for test 4111o1.

Figure 5 shows strain rate as a function of time for test 4111o1. Each black line corresponds to a red dashed line in the y - t diagram in figure 3. The strain rate is a maximum near the impact end and decreases as the distance down the length of the specimen increases.

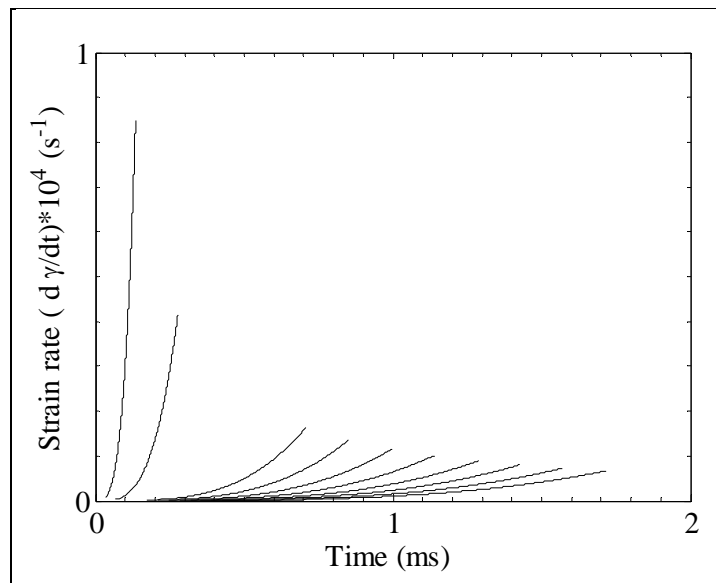


Figure 5. Strain rate as a function of time for test 4111o1.

Three simulations of the experiment were conducted in Presto using different parameter values in the Swanson model. Figure 6 shows the particle trajectories from the experiment with matches from the Presto numerical simulations and Riemann simulation. The Riemann simulation, shown with a solid red line, uses the power-law model. The one-term Swanson model is shown by the dashed blue line with $A_1 = 0.525e6$, $P_1 = -0.16$, and $B_1 = Q_1 = C_1 = R_1 = 0$. The two-term

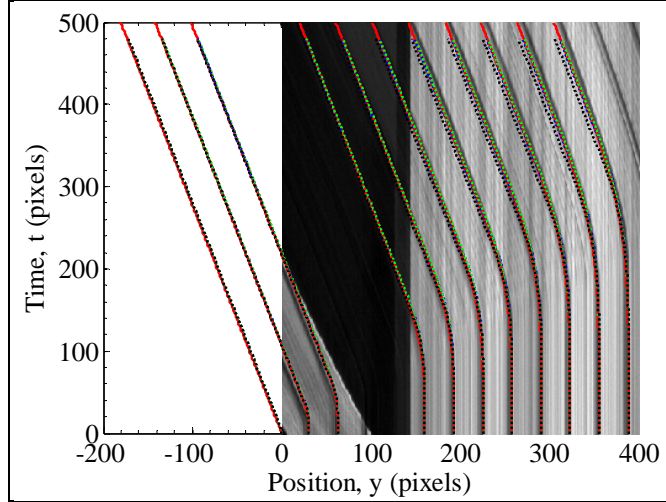


Figure 6. Numerical simulations with experimental results for test 4111o1.

Swanson model is shown by the dashed green line with $A_1 = 0.22e6$, $P_1 = -0.2$, $B_1 = 0.4e6$, $Q_1 = -0.1$, and $C_1 = R_1 = 0$. The three-term Swanson model is shown by the dashed black line with $A_1 = 0.2e6$, $P_1 = -0.2$, $B_1 = 0.4e6$, $Q_1 = -0.1$, $C_1 = 0.2e6$, and $R_1 = 0.2$. Particle trajectories from simulations are seen to match experimental results. Please note a cutoff strain of $\varepsilon_{cut} = 1$ was used to determine the bulk modulus for all the Presto simulations.

Figure 7 shows the true stress along the axial loading direction as a function of log strain for test 4111o1. The same colors for numerical simulations are replicated from figure 6. Each line for each color corresponds to a single line in figure 6. An additional solid black line shows the quasi-static tensile test of a vector 4111 specimen. This figure shows that the Swanson model with each set of parameters matches the power-law model fairly well.

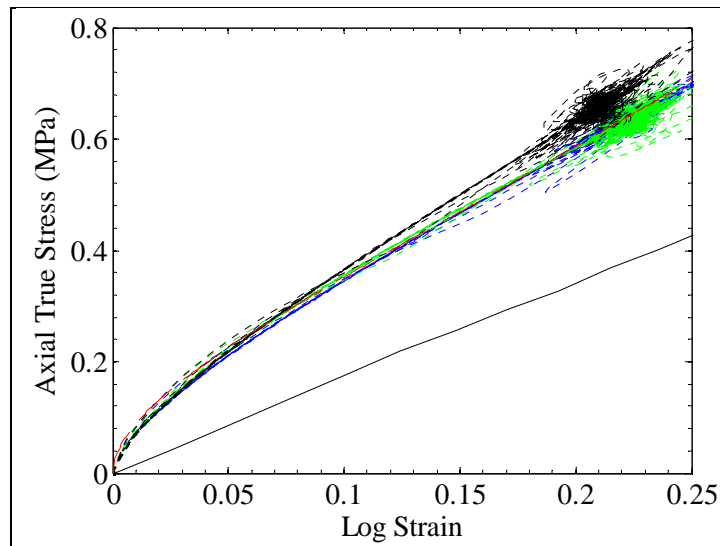


Figure 7. True stress as a function of log strain for test 4111o1.

Figure 8 shows the true axial stress for each Presto simulation as a function of time for each line in figure 7. The numerical simulations are seen to oscillate around the peak stress once the tensile waves have passed a given location. This oscillation can be seen in figure 7 at the peak log strain. This oscillation may be a result of the numerical implementation and is not likely to be indicative of the actual behavior. If the loading velocity is ramped over a longer time to the final loading velocity, the oscillations decrease in magnitude. There is a tradeoff between decreasing the oscillation and matching particle trajectories. There is a small plateau in the axial true stress below 0.2 MPa. This plateau is prevalent in all Presto simulations and may be a result of the numerical implementation.

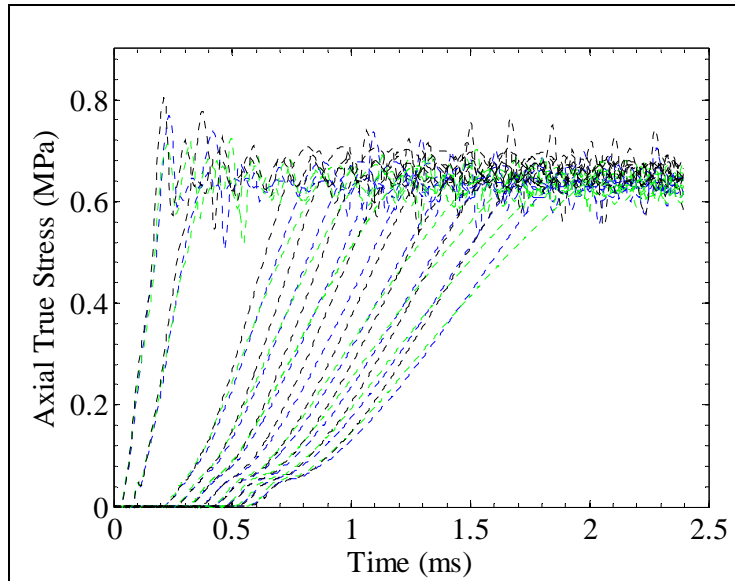


Figure 8. Time history of true stress from numerical simulations for test 4111o1.

8.2 Test 4111o2

Figure 9 shows the y-t diagram for test 4111o2. The loading velocity is 12.2 m/s from the y-t diagram. On top of the y-t diagram are red dashed lines showing particle trajectories obtained from a 1-D analysis using the parameters $n = 0.55$ and $\mu = 1.1$ MPa for the power-law model. The initial strain was $\gamma_0 = 0.031$. The strain at the end of the 1-D analysis was $\gamma_{end} = 0.32$. The largest strain in the y-t diagram was $\gamma_{max} = 1.45$. A white backdrop was used during this particular test to help facilitate the tracking of specimen lines once the flange has moved out of view.

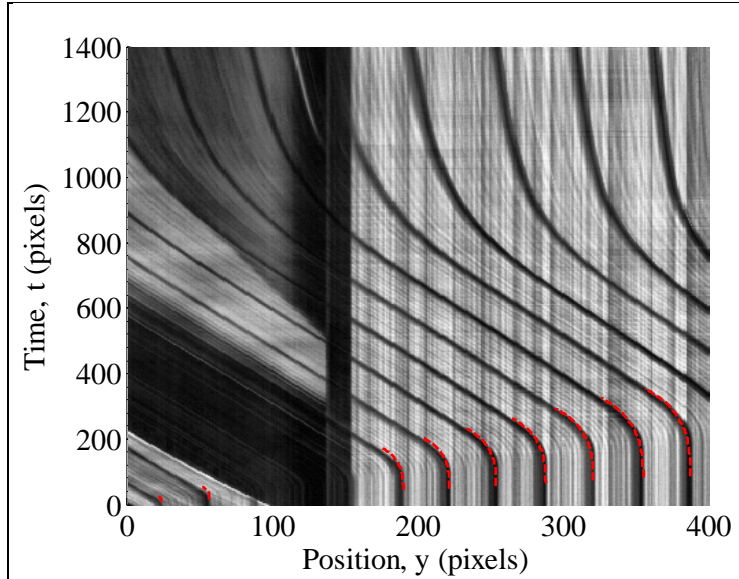


Figure 9. y-t diagram for test 4111o2.

Figure 10 shows the stress-strain relation for test 4111o2 using the power-law model. This dynamic stress-strain relation is a little stiffer than the quasi-static case.

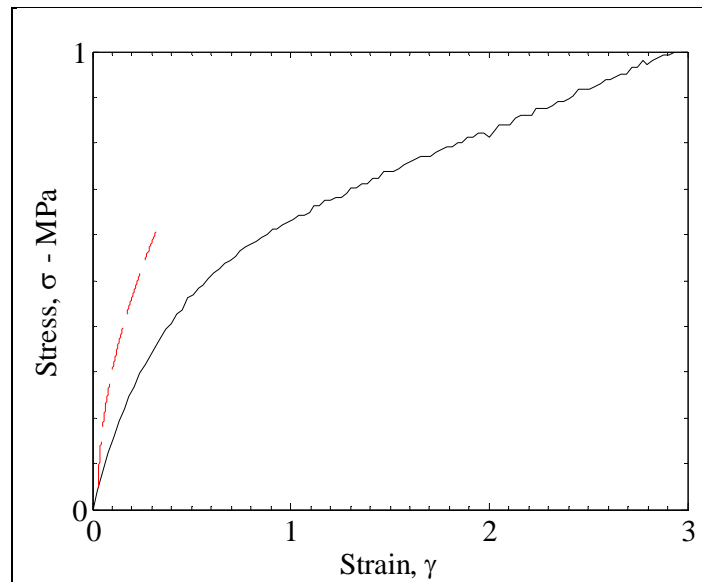


Figure 10. Nominal stress-strain relation for test 4111o2.

Figure 11 shows strain rate as a function of time for test 4111o2. Each black line corresponds to a red dashed line in the y-t diagram. The strain rate is a maximum near the impact end and decreases as the distance down the length of the specimen increases.

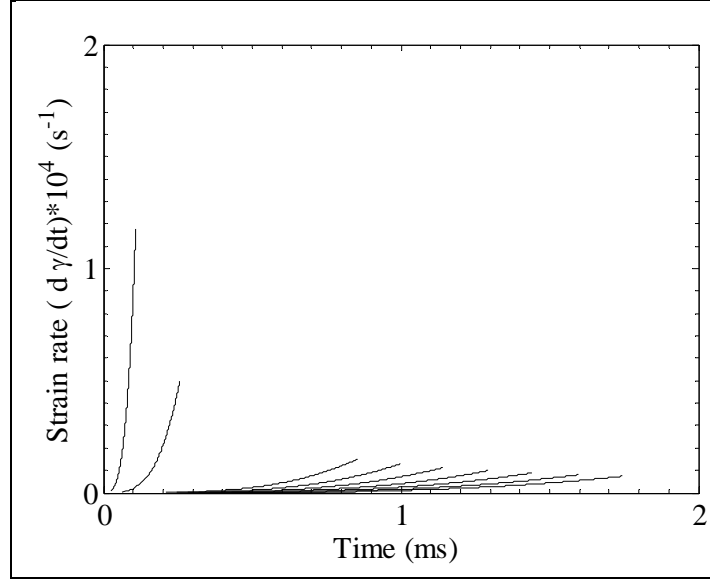


Figure 11. Strain rate as a function of time for test 4111o2.

Three simulations of the experiment were conducted in Presto using different values in the Swanson model for test 4111o2. Figure 12 shows the particle trajectories from the experiment with matches from the Presto numerical simulations with a Riemann simulation. The Riemann simulation, shown with a solid red line, uses the power-law model. The one-term Swanson model is shown by the dashed blue line, with $A_1 = 0.525e6$, $P_1 = -0.16$, and $B_1 = Q_1 = C_1 = R_1 = 0$. The two-term Swanson model is shown by the dashed green line, with $A_1 = 0.22e6$, $P_1 = -0.2$, $B_1 = 0.4e6$, $Q_1 = -0.1$, and $C_1 = R_1 = 0$. The three-term Swanson model is shown by the dashed black line, with $A_1 = 0.2e6$, $P_1 = -0.2$, $B_1 = 0.4e6$, $Q_1 = -0.1$, $C_1 = 0.2e6$, and $R_1 = 0.2$. The numerical simulations match the experiments reasonably well. The Swanson model shown with the black dashed line can be seen to displace to a larger extent than the experiment at latter time near the right side of the y-t diagram.

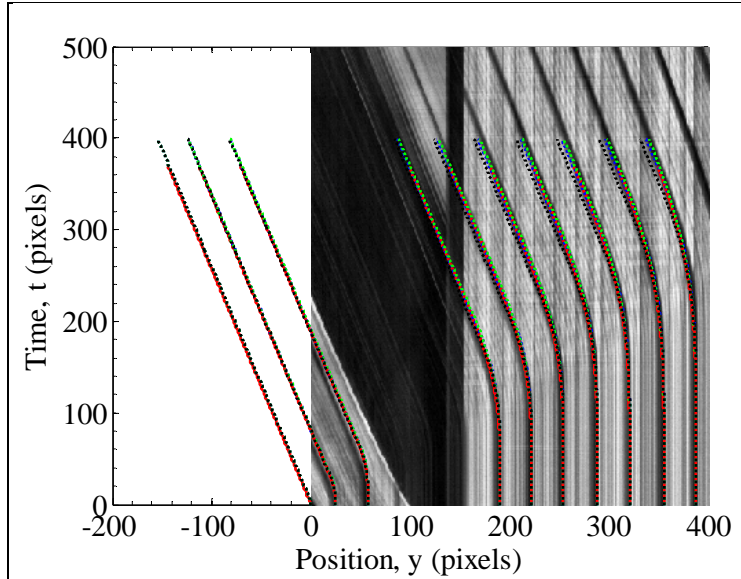


Figure 12. Numerical simulations with experimental results for test 4111o2.

Figure 13 shows the true stress along the axial loading direction as a function of log strain for test 4111o2. The same colors for numerical simulations are replicated from figure 12. Each line for each color corresponds to a single line in figure 12. An additional solid black line shows the quasi-static tensile test of a vector 4111 specimen.

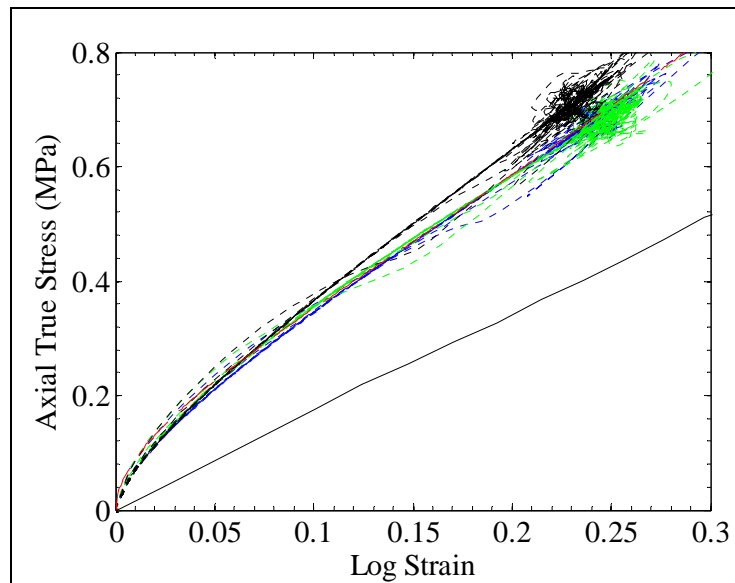


Figure 13. True stress as a function of log strain for test 4111o2.

Figure 14 shows the true axial stress for each Presto simulation as a function of time for each line in figure 12.

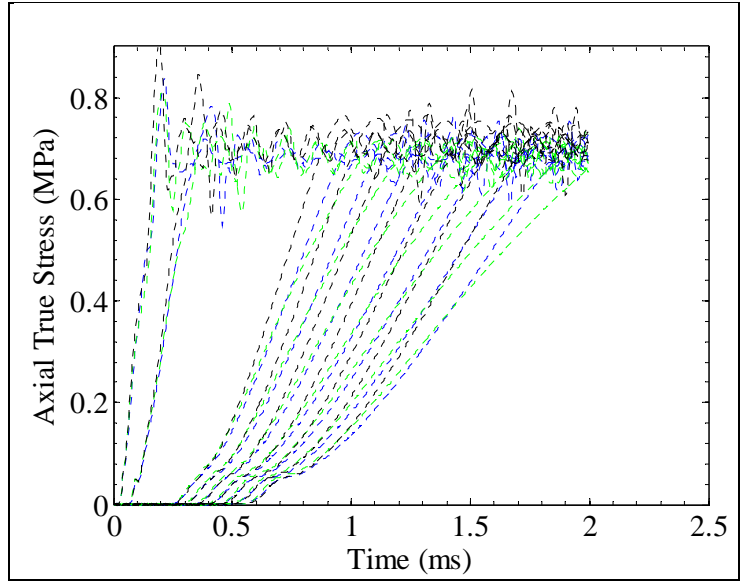


Figure 14. Time history of true stress from numerical simulations for test 4111o2.

9. Vector 4211 Specimens

Vector 4211 specimens are a little stiffer than vector 4111 specimens. Figure 15 shows the summary of nominal stress-strain relations for vector 4211 specimens. With increasing impact velocity, there is an increase in the nominal stress for any given strain.

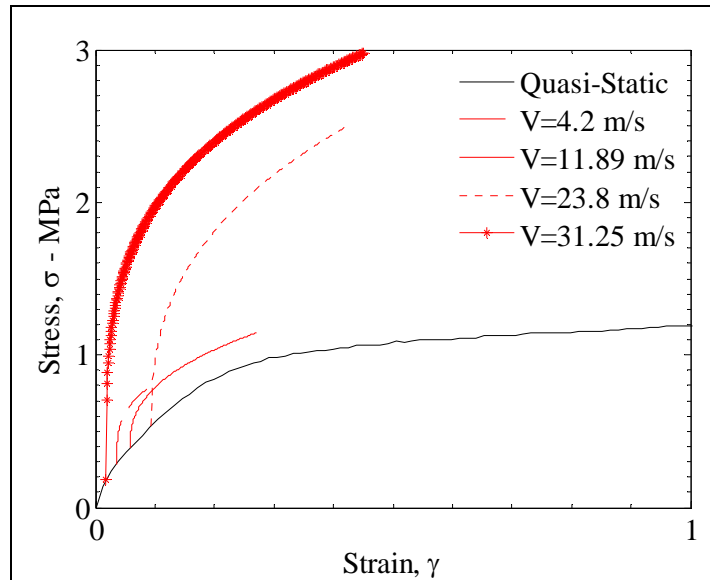


Figure 15. Nominal stress-strain relation for vector 4211 specimens.

9.1 Test 4211o1

Figure 16 shows the y-t diagram for test 4211o1. The loading velocity is 4.2 m/s from the y-t diagram. On top of the y-t diagram are red dashed lines showing particle trajectories obtained from a 1-D analysis using the parameters $n = 0.3$ and $\mu = 1.2\text{MPa}$ for the power-law model. The initial strain was $\gamma_0 = 0.036$. The strain at the end of the 1-D analysis was $\gamma_{end} = 0.087$. The largest strain in the y-t diagram was $\gamma_{max} = 0.17$.

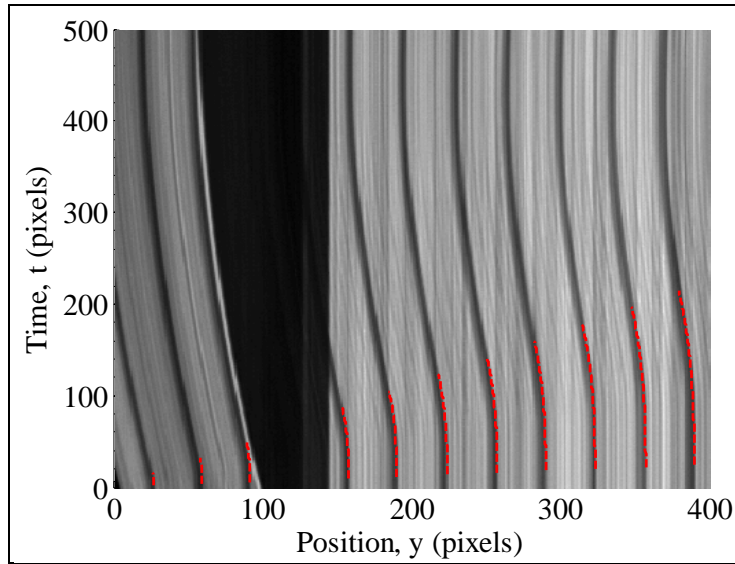


Figure 16. y-t diagram for test 4211o1.

Figure 17 shows the stress-strain relation for test 4211o1 using the power-law model. This dynamic stress-strain relation is initially a little stiffer than the quasi-static case but then begins to soften with a decreasing tangent modulus.

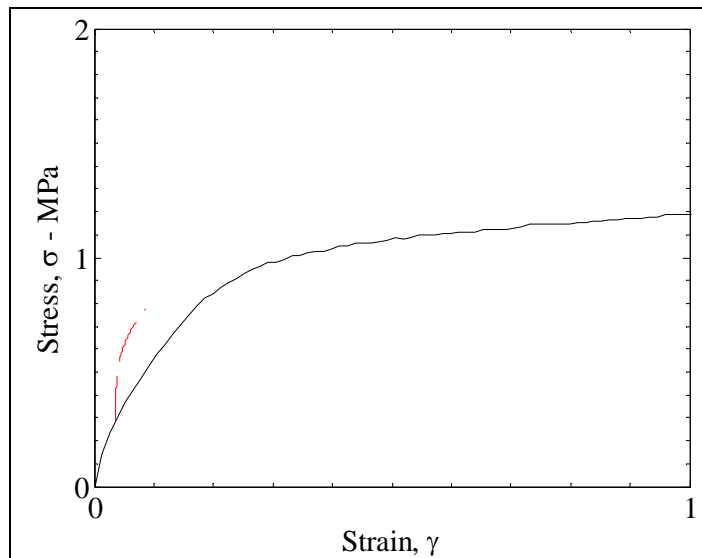


Figure 17. Nominal stress-strain relation for test 4211o1.

Figure 18 shows strain rate as a function of time for test 4211o1. Each black line corresponds to a red dashed line in the y-t diagram. The strain rate is a maximum near the impact end and decreases as the distance down the length of the specimen increases.

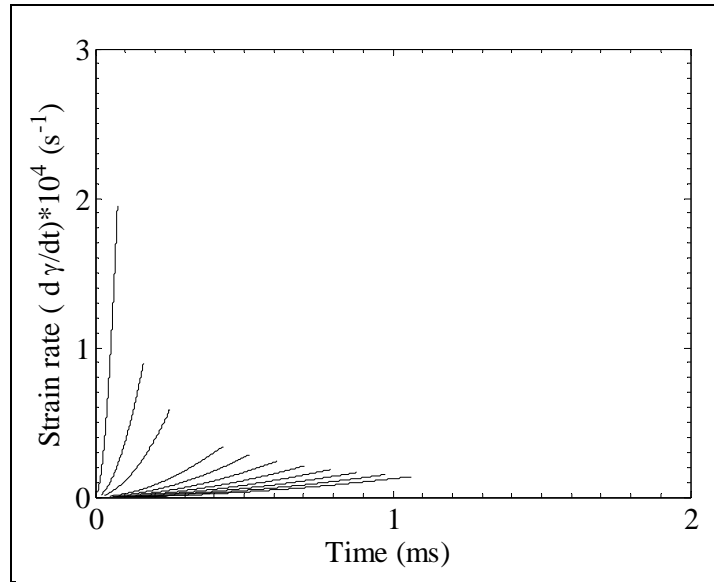


Figure 18. Strain rate for test 4211o1.

Three simulations of the experiment were conducted in Presto using different values in the Swanson model for test 4211o1. Figure 19 shows the particle trajectories from the experiment with matches from the Presto numerical simulations with a Riemann simulation. The Riemann simulation, shown with a solid red line, uses the power-law model. The one-term Swanson model is shown by the dashed blue line, with $A_1 = 0.5e6$, $P_1 = -0.32$, and $B_1 = Q_1 = C_1 = R_1 = 0$. The two-term Swanson model is shown by the dashed green line, with $A_1 = 0.2e6$, $P_1 = -0.36$, $B_1 = 0.55e6$, $Q_1 = -0.17$, and $C_1 = R_1 = 0$. The three-term Swanson model is shown by the dashed black line, with $A_1 = 0.19e6$, $P_1 = -0.36$, $B_1 = 0.55e6$, $Q_1 = -0.17$, $C_1 = 0.19e6$, and $R_1 = 0.36$.

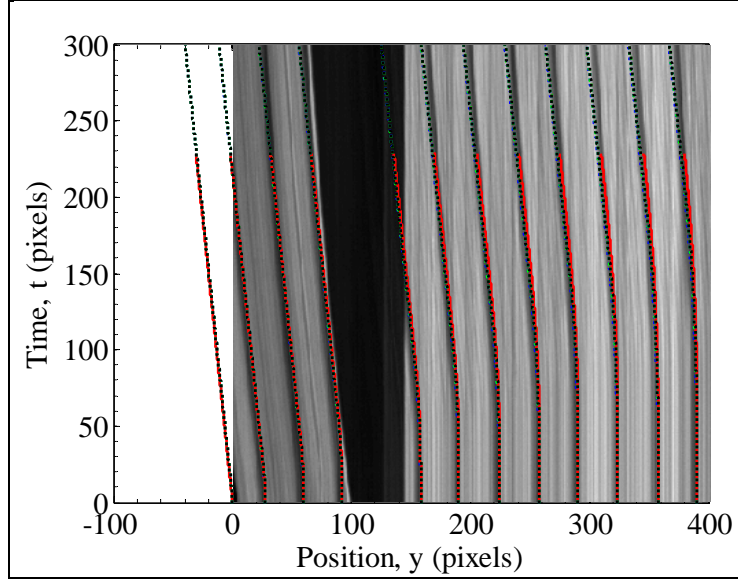


Figure 19. Numerical simulations with experimental results for test 4211o1.

Figure 20 shows the true stress along the axial loading direction as a function of log strain for test 4211o1. The same colors for numerical simulations are replicated from figure 19. Each line for each color corresponds to a single line in figure 19. An additional solid black line shows the quasi-static tensile test of a vector 4211 specimen. Please note that the green dashed lines match the black dashed lines but not the blue or red dashed lines. In the matching process for the stress-strain relation, larger strains were matched but small strains were not. From figure 19, we see little difference between simulations and experiment, yet we see a larger difference in the stress-strain response for each line. This calls into question the use of experiments, which experience only small displacements of nine pixels before a constant state is reached for determining parameters for the Swanson model. We also see from this figure a deviation of the true stress-log strain relation for the Swanson model from the power-law model for the smallest strains (i.e., the initial slopes are not the same); this deviation results from using a finite bulk modulus in the Swanson model in the numerical simulation.

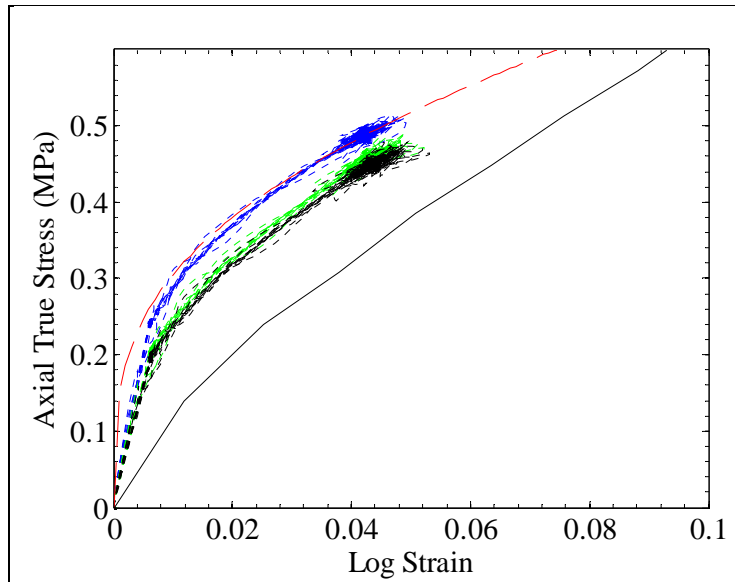


Figure 20. True stress as a function of log strain for test 4211o1.

Figure 21 shows the true axial stress for each Presto simulation as a function of time for each line in figure 19.

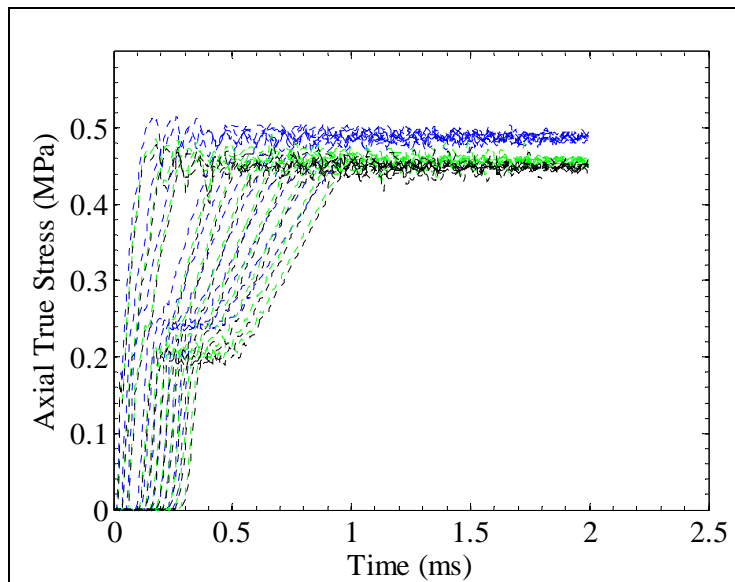


Figure 21. Time history of true stress from numerical simulations for test 4211o1.

9.2 Test 4211o2

Figure 22 shows the y-t diagram for test 4211o2. The loading velocity is 11.89 m/s from the y-t diagram. On top of the y-t diagram are red dashed lines showing particle trajectories obtained from 1-D analysis using the parameters $n=0.4$ and $\mu=1.4\text{MPa}$ for the power-law model. The initial strain was $\gamma_0 = 0.058$. The strain at the end of the 1-D analysis was $\gamma_{end} = 0.27$. The largest strain in the y-t diagram was $\gamma_{max} = 2.07$.

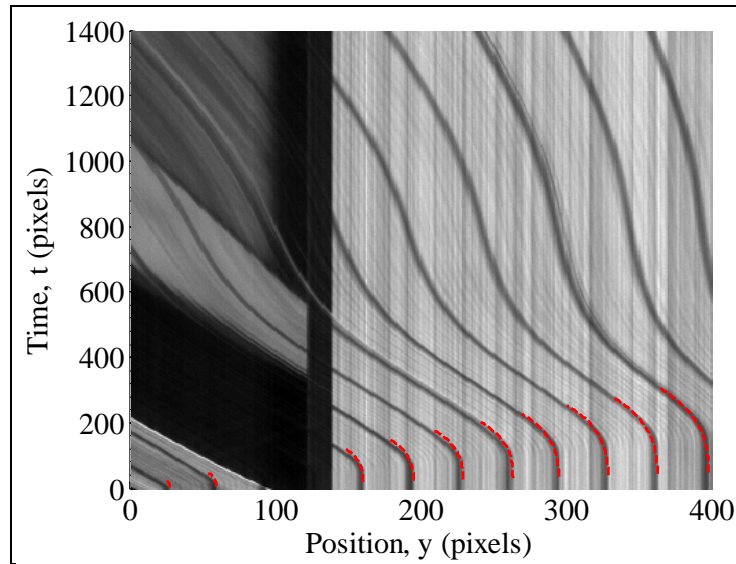


Figure 22. y-t diagram for test 4211o2.

Figure 23 shows the stress-strain relation for test 4211o2 using the power-law model. This dynamic stress-strain relation is a little stiffer than the quasi-static case.

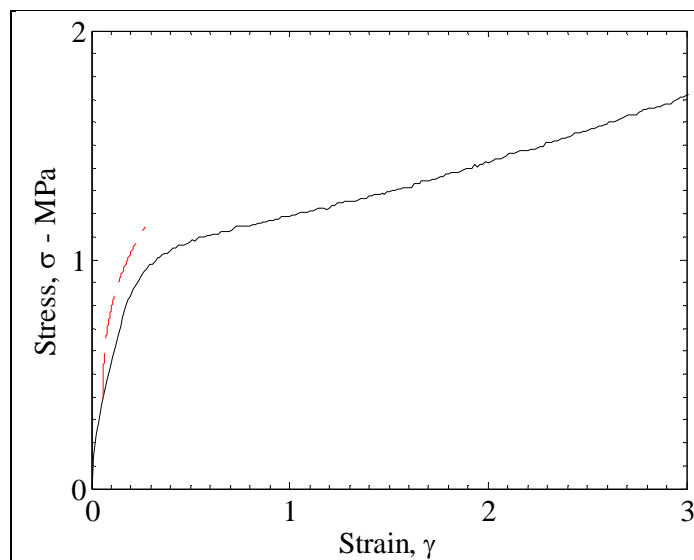


Figure 23. Nominal stress-strain relation for test 4211o2.

Figure 24 shows strain rate as a function of time for test 4211o2. Each black line corresponds to a red dashed line in the y-t diagram. The strain rate is a maximum near the impact end and decreases as the distance down the length of the specimen increases.

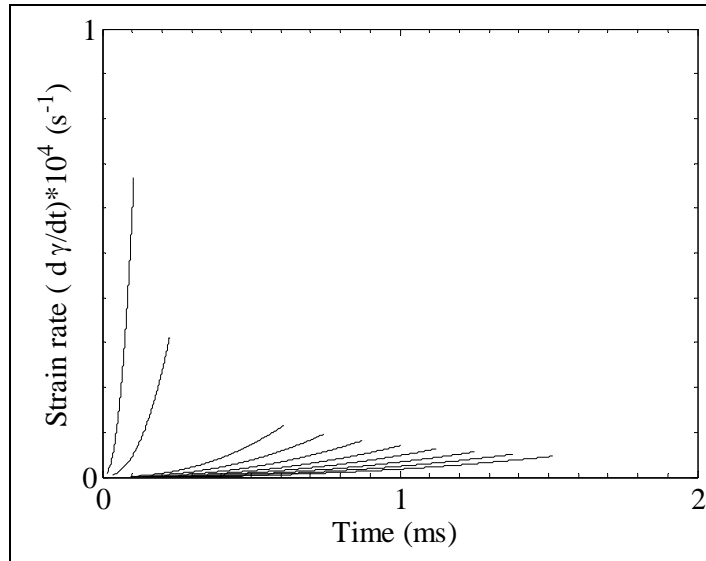


Figure 24. Strain rate as a function of time for test 4211o2.

Three simulations of the experiment were conducted in Presto using different values in the Swanson model for test 4211o2. Figure 25 shows the particle trajectories from the experiment with matches from the Presto numerical simulations with a Riemann simulation. The Riemann simulation, shown with a solid red line, uses the power-law model. The one-term Swanson model is shown by the dashed blue line, with $A_1 = 0.55e6$, $P_1 = -0.28$, and $B_1 = Q_1 = C_1 = R_1 = 0$. The two-term Swanson model is shown by the dashed green line, with $A_1 = 0.2e6$, $P_1 = -0.36$, $B_1 = 0.55e6$, $Q_1 = -0.15$, and $C_1 = R_1 = 0$. The three-term Swanson model is shown by the dashed black line, with $A_1 = 0.22e6$, $P_1 = -0.36$, $B_1 = 0.55e6$, $Q_1 = -0.15$, $C_1 = 0.22e6$, and $R_1 = 0.36$.

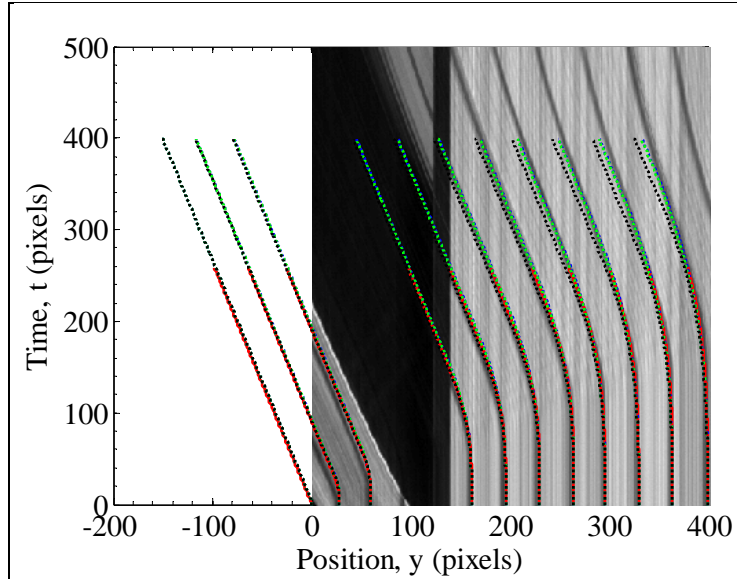


Figure 25. Numerical simulations with experimental results for test 4211o2.

Figure 26 shows the true stress along the axial loading direction as a function of log strain for test 4211o2. The same colors for numerical simulations are replicated from figure 25. Each line for each color corresponds to a single line in figure 25. An additional solid black line shows the quasi-static tensile test of a vector 4211 specimen. Please note that the black dashed line for the stress-strain relation is stiffer than the other Swanson fits and power-law fit. As such, the particle trajectories in figure 25 are seen to displace a greater amount at later times for a few lines at the right edge of the y-t diagram.

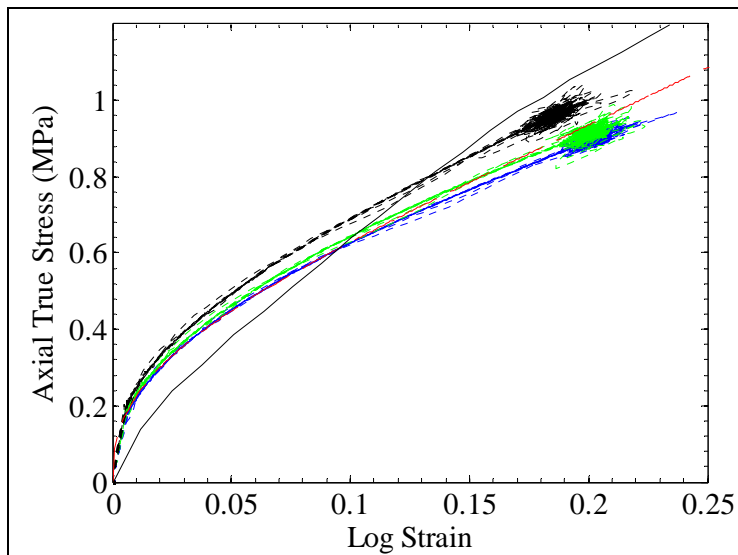


Figure 26. True stress as a function of log strain for test 4211o2.

Figure 27 shows the true axial stress for each Presto simulation as a function of time for each line in figure 25.

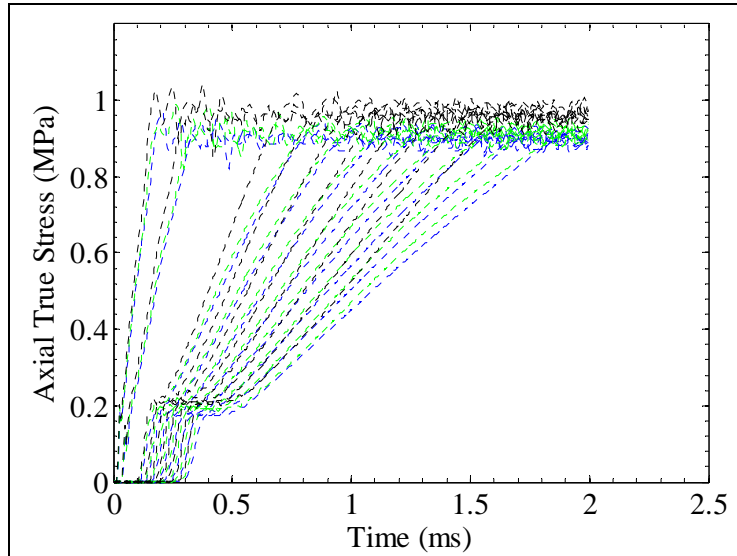


Figure 27. Time history of true stress from numerical simulations for test 4211o2.

9.3 Test 4211o3

Figure 28 shows the y-t diagram for test 4211o3. The loading velocity is 23.8 m/s from the y-t diagram. On top of the y-t diagram are red dashed lines showing particle trajectories obtained from a 1-D analysis using the parameters $n = 0.38$ and $\mu = 3$ MPa for the power-law model. The initial strain was $\gamma_0 = 0.094$. The strain at the end of the 1-D analysis was $\gamma_{end} = 0.419$. The largest strain in the y-t diagram was $\gamma_{max} = 3.97$.

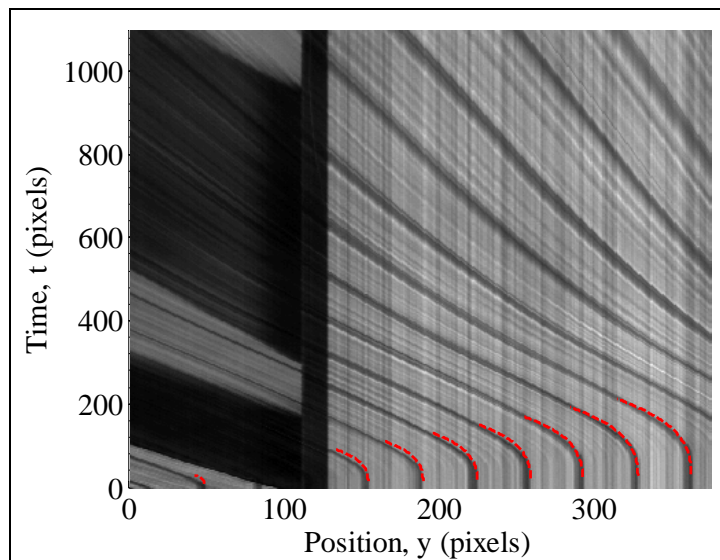


Figure 28. y-t diagram for test 4211o3.

Figure 29 shows the stress-strain relation for test 4211o3 using the power-law model. This dynamic stress-strain relation is a little stiffer than the quasi-static case.

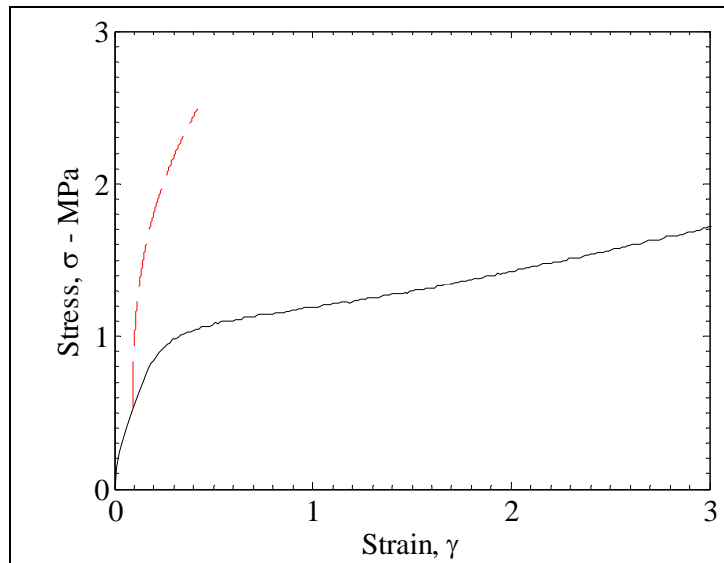


Figure 29. Nominal stress-strain relation for test 4211o3.

Figure 30 shows strain rate as a function of time for test 4211o3. Each black line corresponds to a red dashed line in the y - t diagram. The strain rate is a maximum near the impact end and decreases as the distance down the length of the specimen increases.

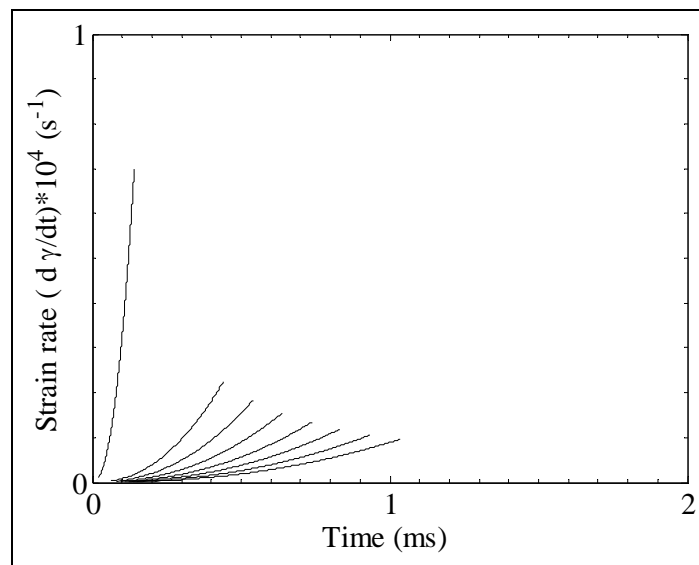


Figure 30. Strain rate as a function of time for test 4211o3.

Three simulations of the experiment were conducted in Presto using different values in the Swanson model for test 4211o3. Figure 31 shows the particle trajectories from the experiment with matches from the Presto numerical simulations with a Riemann simulation. The Riemann

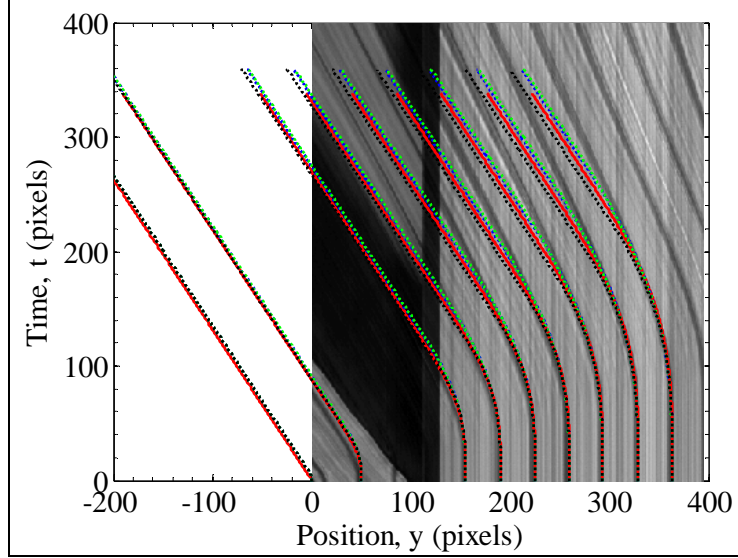


Figure 31. Numerical simulations with experimental results for test 4211o3.

simulation, shown with a solid red line, uses the power-law model. The one-term Swanson model is shown by the dashed blue line, with $A_1 = 1.25e6$, $P_1 = -0.28$, and $B_1 = Q_1 = C_1 = R_1 = 0$. The two-term Swanson model is shown by the dashed green line with $A_1 = 0.6e6$, $P_1 = -0.33$, $B_1 = 1e6$, $Q_1 = -0.15$, and $C_1 = R_1 = 0$. The three-term Swanson model is shown by the dashed black line, with $A_1 = 0.58e6$, $P_1 = -0.33$, $B_1 = 1e6$, $Q_1 = -0.15$, $C_1 = 0.58e6$, and $R_1 = 0.33$. There is significant deviation in the simulations from experiment for times beyond 180 pixels.

Figure 32 shows the true stress along the axial loading direction as a function of log strain for test 4211o3. The same colors for numerical simulations are replicated from figure 31. Each line for each color corresponds to a single line in figure 31. An additional solid black line shows the quasi-static tensile test of a vector 4211 specimen. While these stress-strain relations match each other, they are not the stress-strain relations experienced in the specimen given the difference from the experimental particle trajectory in figure 31.

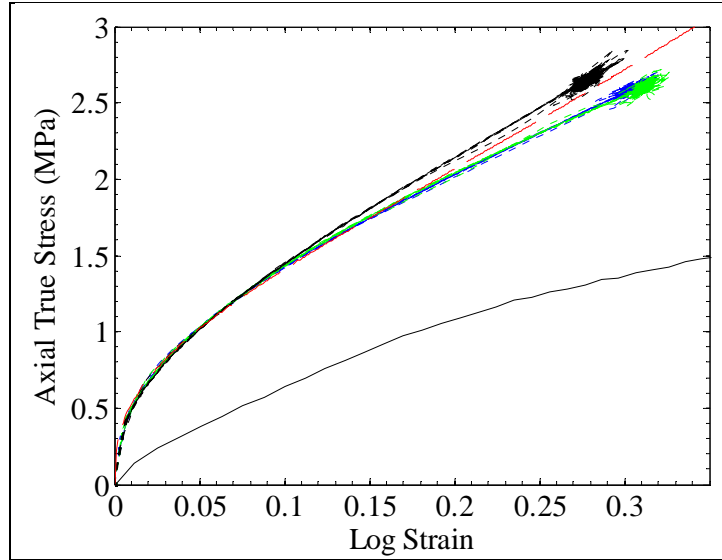


Figure 32. True stress as a function of log strain for test 4211o3.

Figure 33 shows the true axial stress for each Presto simulation as a function of time for each line in figure 31.

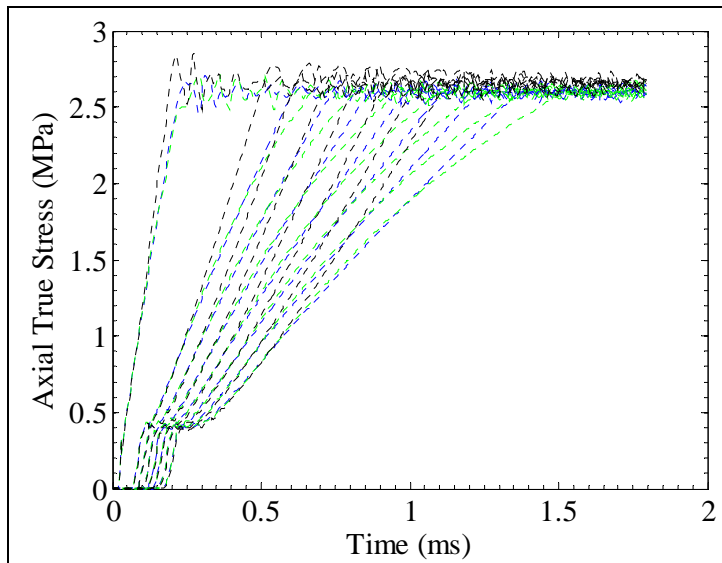


Figure 33. Time history of true stress from numerical simulations for test 4211o3.

9.4 Test 4211o4

Figure 34 shows the y-t diagram for test 4211o4. The loading velocity is 31.25 m/s from the y-t diagram. On top of the y-t diagram are red dashed lines showing particle trajectories obtained from a 1-D analysis using the parameters $n = 0.27$ and $\mu = 3.5$ MPa for the power-law model. The initial strain was $\gamma_0 = 0.018$. The strain at the end of the 1-D analysis was $\gamma_{end} = 0.451$. The largest strain in the y-t diagram was $\gamma_{max} = 1.17$.

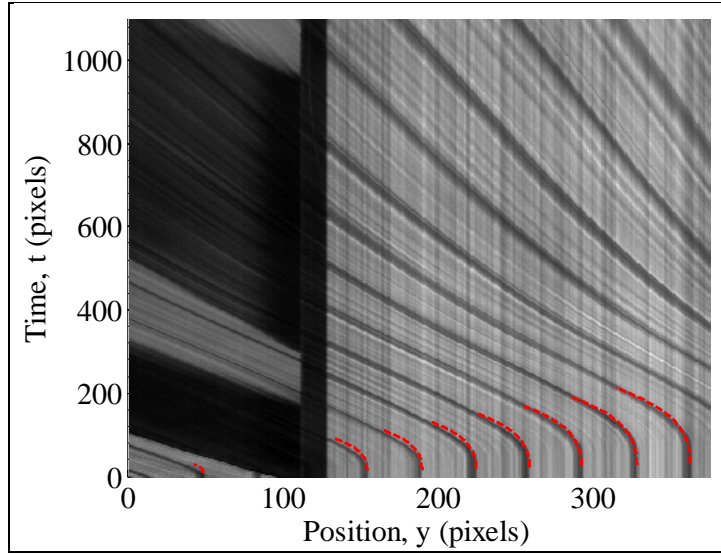


Figure 34. y-t diagram for test 4211o4.

Figure 35 shows the stress-strain relation for test 4211o4 using the power-law model. This dynamic stress-strain relation is a little stiffer than the quasi-static case.

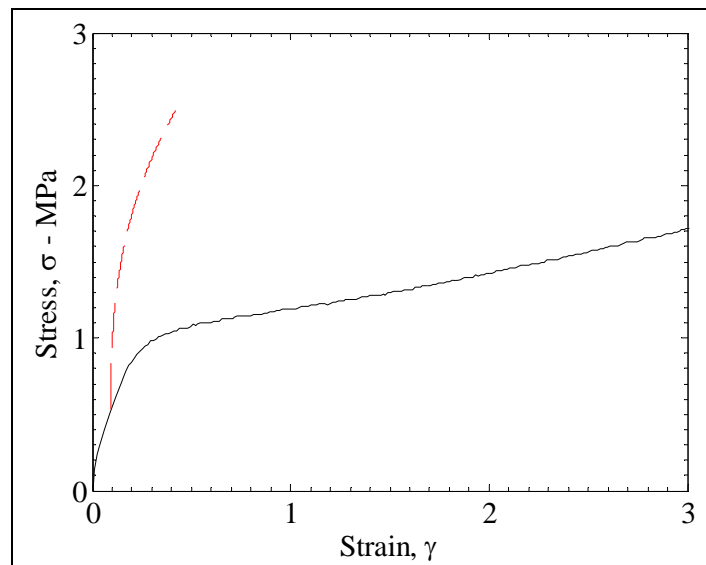


Figure 35. Nominal stress-strain relation for test 4211o4.

Figure 36 shows strain rate as a function of time for test 4211o4. Each black line corresponds to a red dashed line in the y-t diagram. The strain rate is a maximum near the impact end and decreases as the distance down the length of the specimen increases.

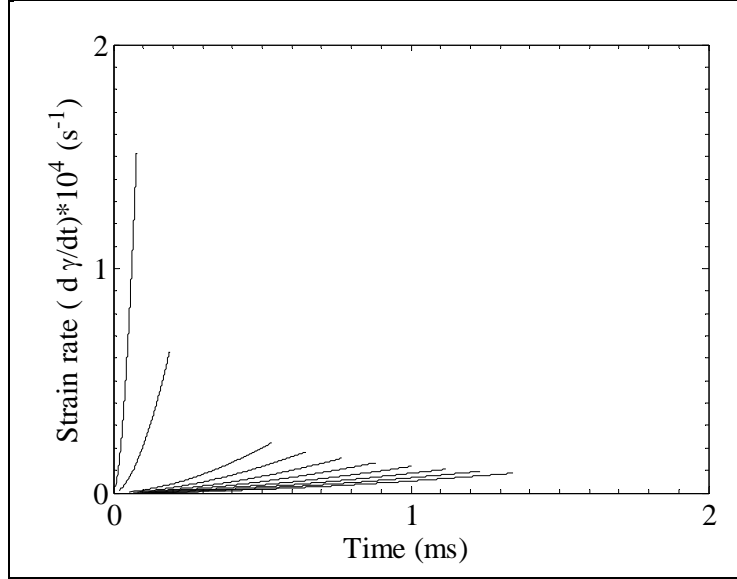


Figure 36. Strain rate as a function of time for test 4211o4.

Three simulations of the experiment were conducted in Presto using different values in the Swanson model for test 4211o4. Figure 37 shows the particle trajectories from the experiment with matches from the Presto numerical simulations with a Riemann simulation. The Riemann simulation, shown with a solid red line, uses the power-law model. The one-term Swanson model is shown by the dashed blue line, with $A_1 = 1.5e6$, $P_1 = -0.33$, and $B_1 = Q_1 = C_1 = R_1 = 0$. The two-term Swanson model is shown by the dashed green line, with $A_1 = 0.7e6$, $P_1 = -0.4$, $B_1 = 1.6e6$, $Q_1 = -0.1$, and $C_1 = R_1 = 0$. The three-term Swanson model is shown by the dashed black line, with $A_1 = 0.6e6$, $P_1 = -0.4$, $B_1 = 1.6e6$, $Q_1 = -0.1$, $C_1 = 0.6e6$, and $R_1 = 0.4$. The black dashed lines are seen to deviate significantly from the experiment after a time of 200 pixels.

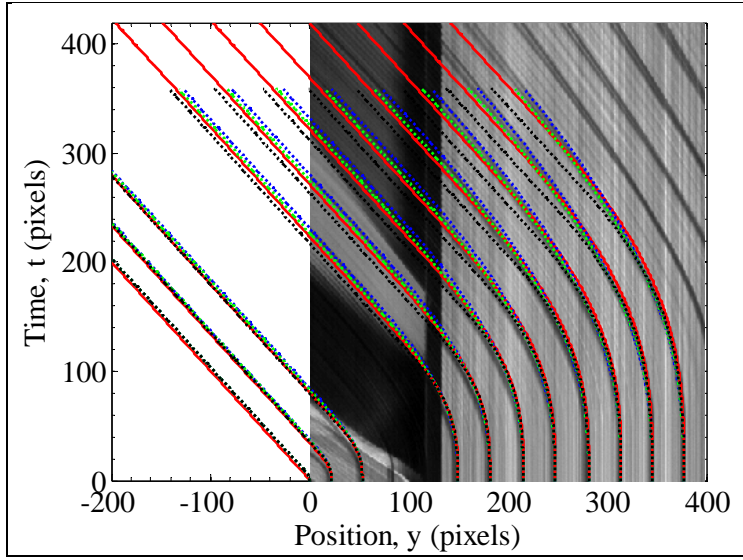


Figure 37. Numerical simulations with experimental results for test 4211o4.

Figure 38 shows the true stress along the axial loading direction as a function of log strain for test 4211o4. The same colors for numerical simulations are replicated from figure 37. Each line for each color corresponds to a single line in figure 37. An additional solid black line shows the quasi-static tensile test of a vector 4211 specimen.

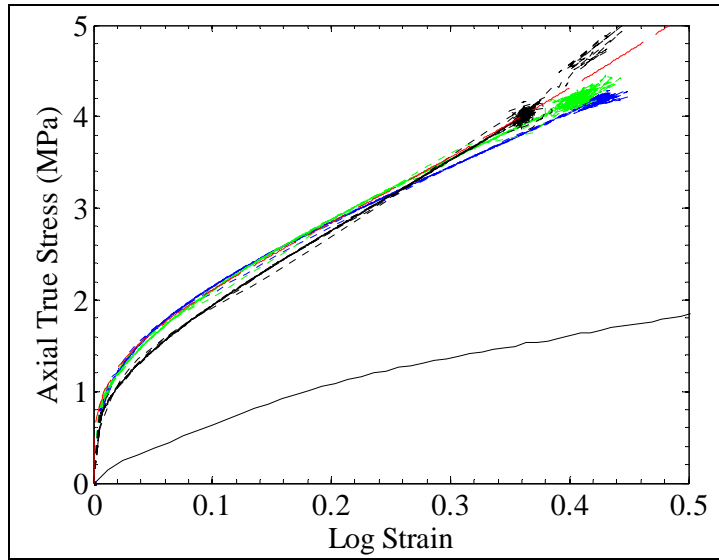


Figure 38. True stress as a function of log strain for test 4211o4.

Figure 39 shows the true axial stress for each Presto simulation as a function of time for each line in figure 37. Please note the increase in stress near the end of the simulation is a result of the reflection for the silent boundary.

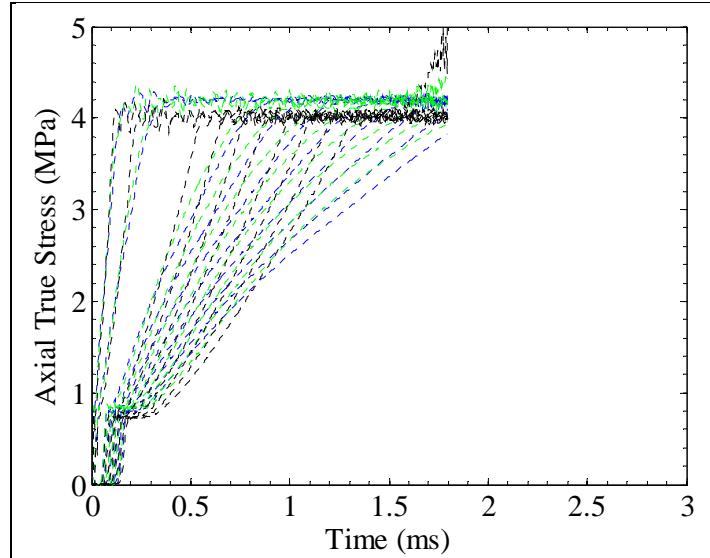


Figure 39. Time history of true stress from numerical simulations for test 4211o4.

10. Vector 4411 Specimens

Vector 4411 specimens are the stiffest of the three batches. Localization in deformation occurs during the impact experiment when the impact velocity is above a threshold. This localization negates the validity of the closed-form solution using the power-law model. The power-law model is applied to all four tests, but only the nominal stress-strain relations for tests 4411o1 and 4411o2 are shown in figure 40 since localization does not appear in these tests. Large stresses are predicted by the power-law model compared to quasi-static tests. The power-law model captures particle trajectories through only a few pixels. This small deformation does raise issue with the accuracy of the power-law match. Results are shown to estimate the stress-strain relation. Future tests are needed to explore particle trajectories by using a larger pixel-to-meter resolution.

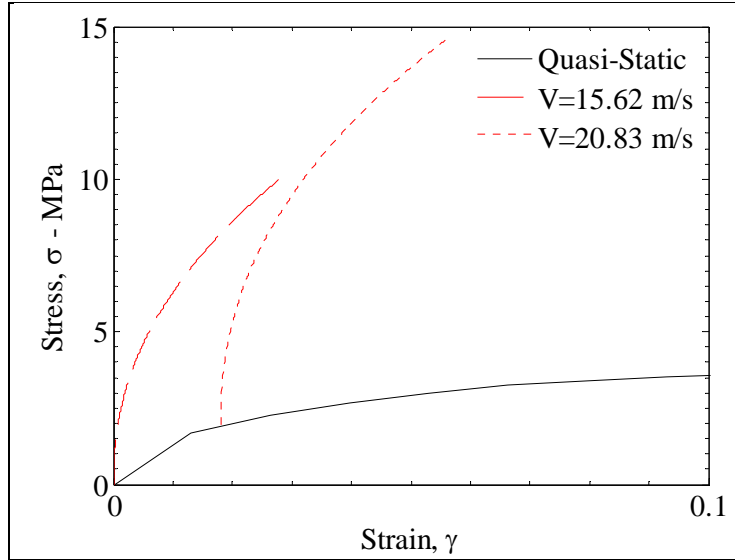


Figure 40. Summary of stress-strain relations for tests 4411o1 and 4411o2.

10.1 Test 4411o1

Figure 41 shows the y-t diagram for test 4411o1. The loading velocity is 15.62 m/s from the y-t diagram. On top of the y-t diagram are red dashed lines showing particle trajectories obtained from a 1-D analysis using the parameters $n=0.45$ and $\mu=50\text{MPa}$ for the power-law model. The initial strain was $\gamma_0 = 0.0$. The strain at the end of the 1-D analysis was $\gamma_{end} = 0.0278$. The largest strain in the y-t diagram was $\gamma_{max} = 0.0278$.

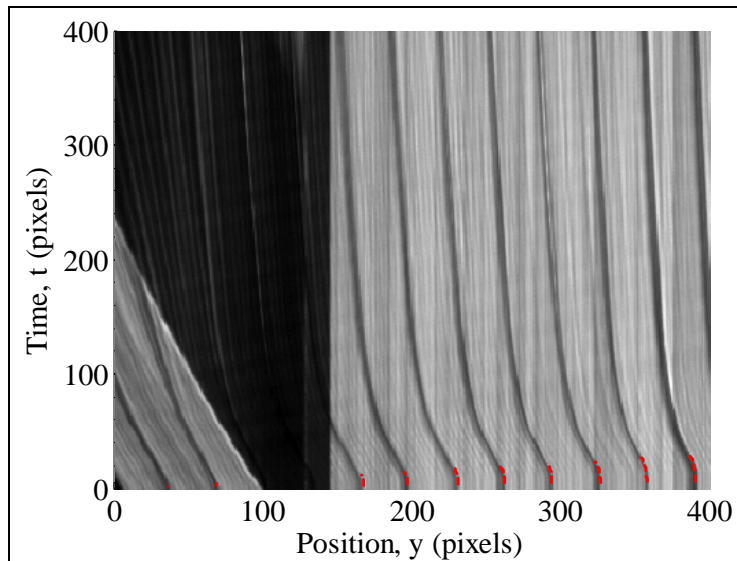


Figure 41. y-t diagram for test 4411o1.

Figure 42 shows the stress-strain relation for test 4411o1 using the power-law model. This dynamic stress-strain relation is stiffer than the quasi-static case and reaches a higher peak stress. These results are from a matching process where the total displacement is a few pixels.

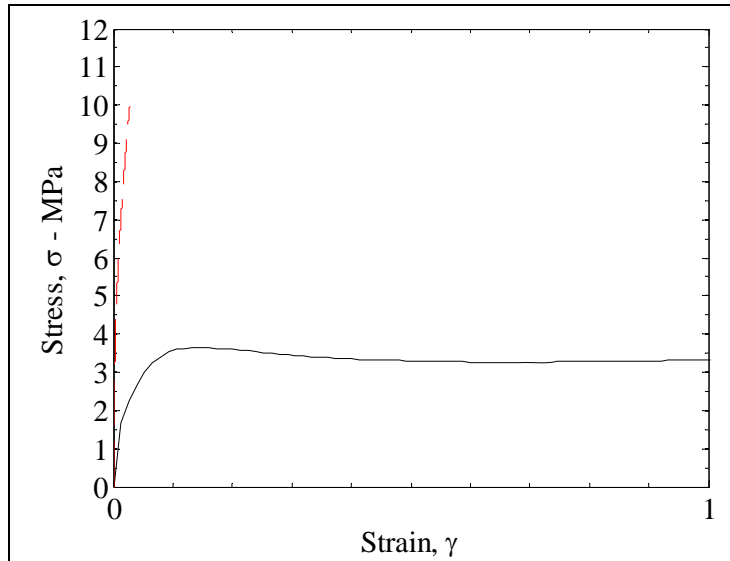


Figure 42. Nominal stress-strain relation for test 4411o1.

Figure 43 shows strain rate as a function of time for test 4411o1. Each black line corresponds to a red dashed line in the y - t diagram. The strain rate is a maximum near the impact end and decreases as the distance down the length of the specimen increases.

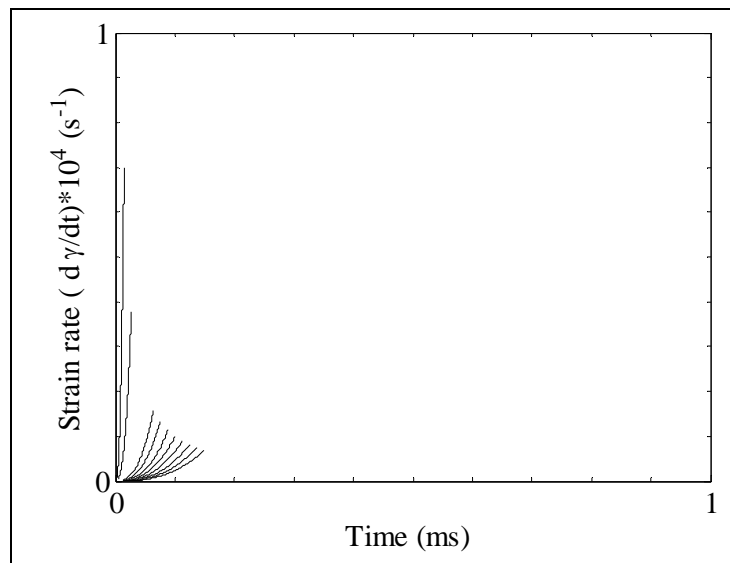


Figure 43. Strain rate as function of time for test 4411o1.

Three simulations of the experiment were conducted in Presto using different values in the Swanson model. Figure 44 shows the particle trajectories from the experiment with matches from the Presto numerical simulations with a Riemann simulation. The Riemann simulation, shown with a solid red line, uses the power-law model. The one-term Swanson model is shown by the dashed blue line, with $A_1 = 17.5e6$, $P_1 = -0.27$, and $B_1 = Q_1 = C_1 = R_1 = 0$. The two-term Swanson model is shown by the dashed green line, with $A_1 = 10.5e6$, $P_1 = -0.3$, $B_1 = 5e6$, $Q_1 = -0.25$, and $C_1 = R_1 = 0$. The three-term Swanson model is shown by the dashed black line, with $A_1 = 12e6$, $P_1 = -0.3$, $B_1 = 5e6$, $Q_1 = -0.25$, $C_1 = 12e6$, and $R_1 = 0.3$. Note that the reflection from the fixed boundary is not taken into account in the numerical simulation, hence the discrepancy between experiment and simulation.

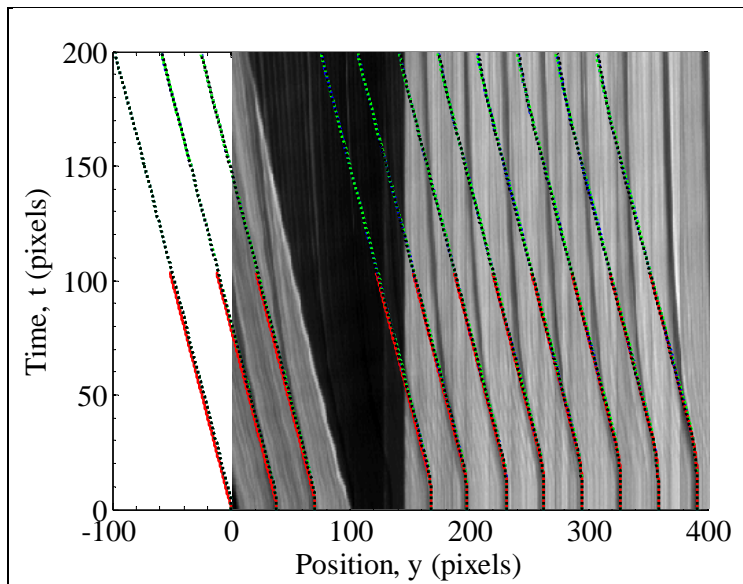


Figure 44. Numerical simulations with experimental results for test 4411o1.

Figure 45 shows the true stress along the axial loading direction as a function of log strain for test 4411o1. The same colors for numerical simulations are replicated from figure 44. Each line for each color corresponds to a single line in figure 44. An additional solid black line shows the quasi-static tensile test of a vector 4411 specimen. Please note the large discrepancy of stress of the dashed black lines from the stress provided from the power-law model results from choosing parameters to match the power-law model at larger strains.

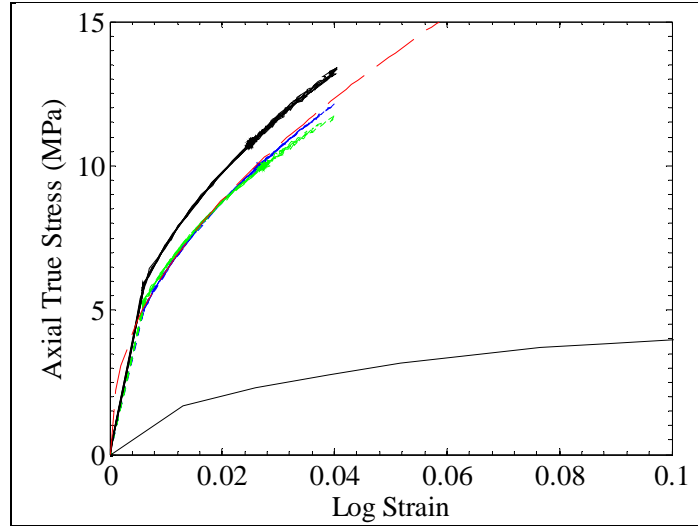


Figure 45. True stress as a function of log strain for test 4411o1.

Figure 46 shows the true axial stress for each Presto simulation as a function of time for each line in figure 44.

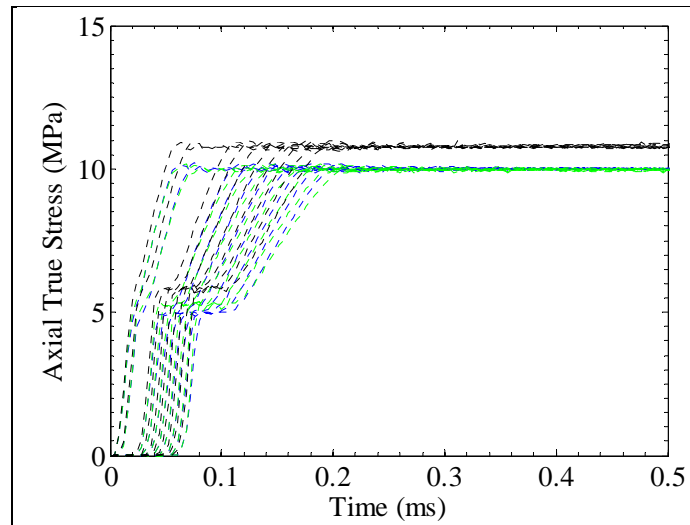


Figure 46. Time history of true stress from numerical simulations for test 4411o1.

10.2 Test 4411o2

Figure 47 shows the y-t diagram for test 4411o2. The loading velocity is 20.83 m/s from the y-t diagram. On top of the y-t diagram are red dashed lines showing particle trajectories obtained from a 1-D analysis using the parameters $n = 0.45$ and $\mu = 55$ MPa for the power-law model. The initial strain was $\gamma_0 = 0.018$. The strain at the end of the 1-D analysis was $\gamma_{end} = 0.056$. The largest strain in the y-t diagram was $\gamma_{max} = 0.95$. These results are from a matching process where the total displacement is a few pixels. Note the apparent localized deformation near the impact point.

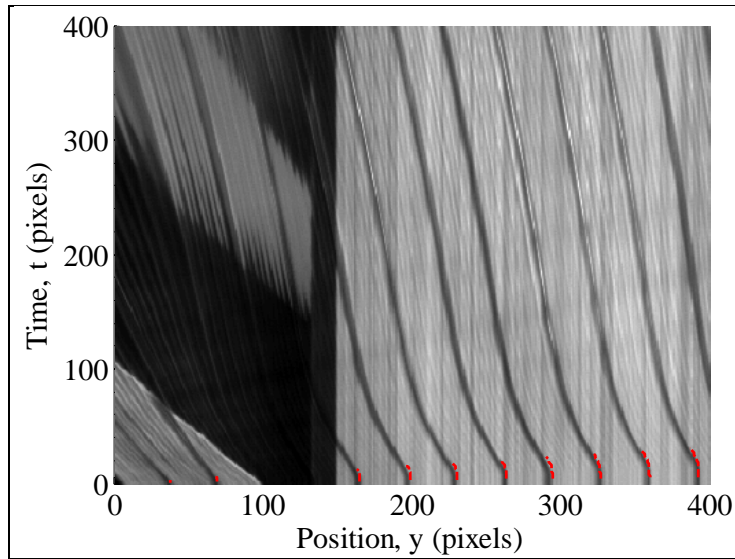


Figure 47. y-t diagram for test 4411o2.

Figure 48 shows the stress-strain relation for test 4411o2 using the power-law model. This dynamic stress-strain relation is stiffer than the quasi-static case and reaches a higher peak stress. This may not be the actual stress-strain relation due to the displacement of only a few pixels and localization at impact point.

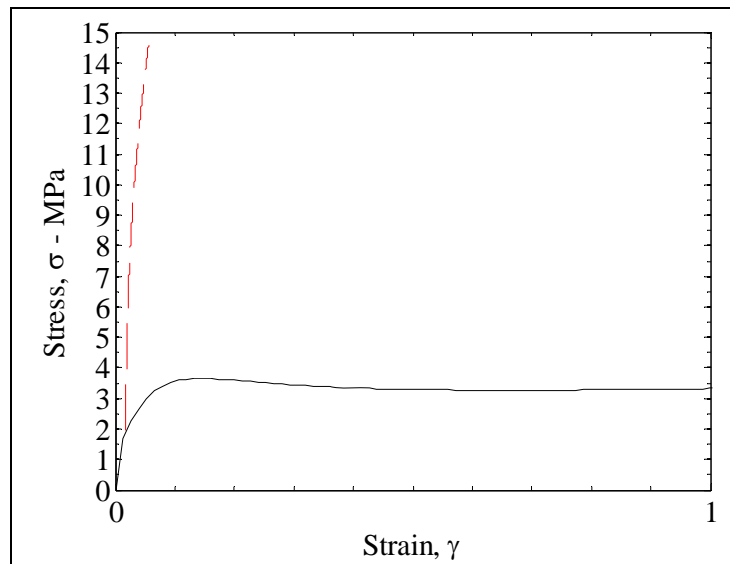


Figure 48. Nominal stress-strain relation for test 4411o2.

Figure 49 shows strain rate as a function of time for test 4411o2. Each black line corresponds to a red dashed line in the y-t diagram. The strain rate is a maximum near the impact end and decreases as the distance down the length of the specimen increases.

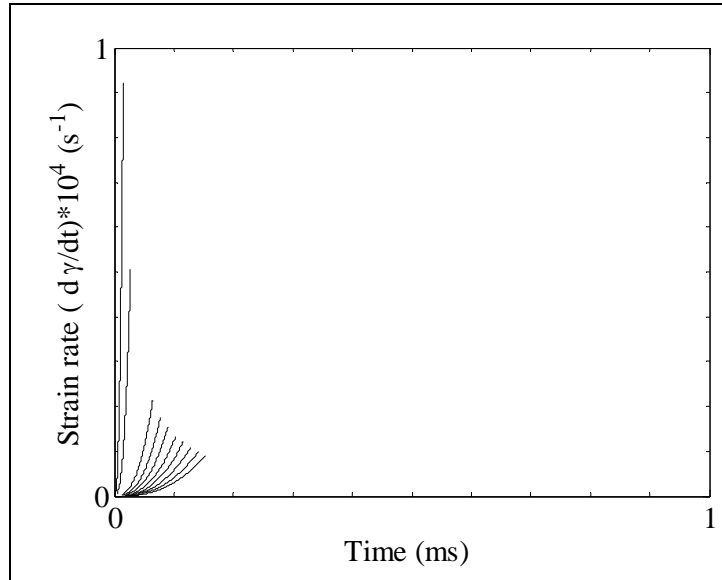


Figure 49. Strain rate as a function of time for test 4411o2.

Three simulations of the experiment were conducted in Presto using different values in the Swanson model. Figure 50 shows the particle trajectories from the experiment with matches from the Presto numerical simulations with a Riemann simulation. The Riemann simulation, shown with a solid red line, uses the power-law model. The one-term Swanson model is shown by the dashed blue line, with $A_1 = 19.5e6$, $P_1 = -0.27$, and $B_1 = Q_1 = C_1 = R_1 = 0$. The two-term Swanson model is shown by the dashed green line, with $A_1 = 15.5e6$, $P_1 = -0.27$, $B_1 = 4.8e6$, $Q_1 = -0.25$, and $C_1 = R_1 = 0$. The three-term Swanson model is shown by the dashed black line, with $A_1 = 15e6$, $P_1 = -0.27$, $B_1 = 4.8e6$, $Q_1 = -0.25$, $C_1 = 15e6$, and $R_1 = 0.27$. Please note the simulation does not account for the fixed boundary in the experiment.

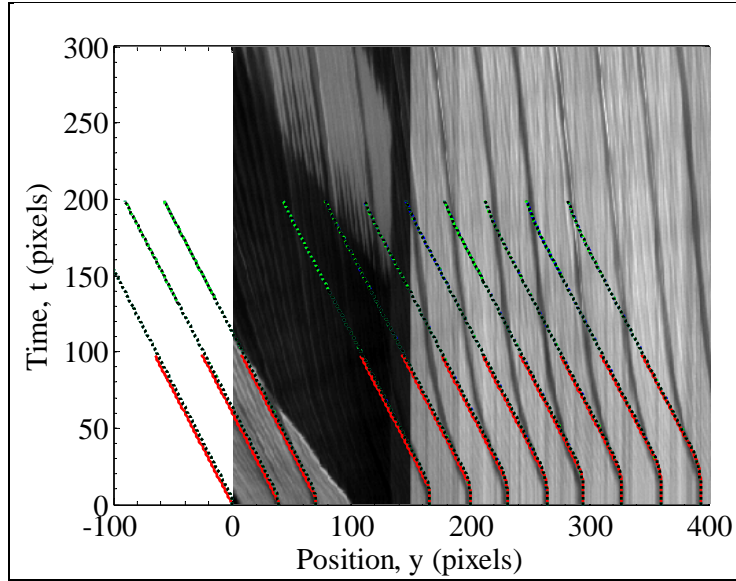


Figure 50. Numerical simulations with experimental results for test 4411o2.

Figure 51 shows the true stress along the axial loading direction as a function of log strain for test 4411o2. The same colors for numerical simulations are replicated from figure 50. Each line for each color corresponds to a single line in figure 50. An additional solid black line shows the quasi-static tensile test of a vector 4411 specimen. The initial slopes do not match since the numerical simulations for the Swanson model provide a finite bulk modulus.

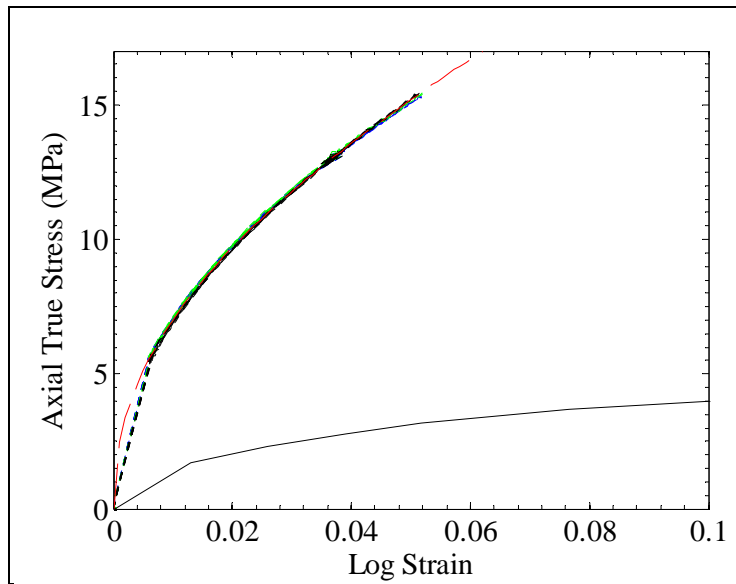


Figure 51. True stress as a function of log strain for test 4411o2.

Figure 52 shows the true axial stress for each Presto simulation as a function of time for each line in figure 50.

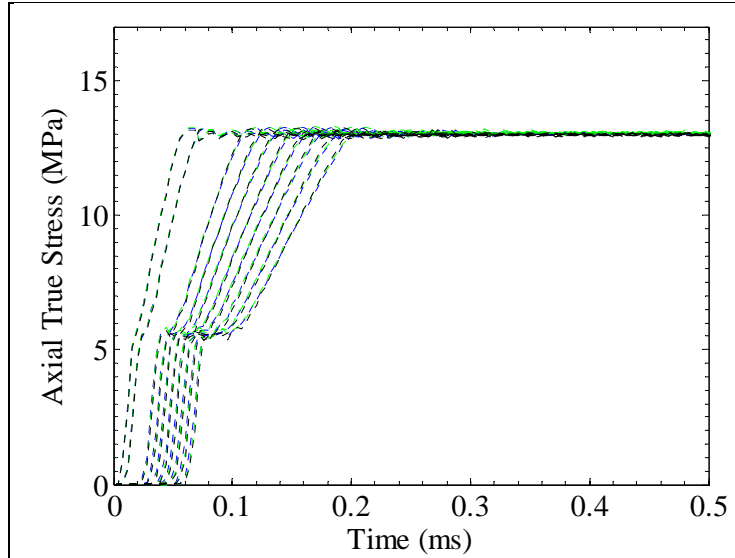


Figure 52. Time history of true stress from numerical simulations for test 4411o2.

10.3 Test 4411o3

Figure 53 shows the y-t diagram for test 4411o3. The loading velocity is difficult to measure from the y-t diagram. On top of the y-t diagram are red dashed lines showing particle trajectories obtained from a 1-D analysis using the parameters $n = 0.4$ and $\mu = 55$ MPa for the power-law model. The initial strain was $\gamma_0 = 0.009$. The strain at the end of the 1-D analysis was $\gamma_{end} = 0.031$. The largest strain in the y-t diagram was $\gamma_{max} = 0.04$. Here localization is evident at the impact point, where the velocity near the impact point is much greater than the final velocity of the lines near the right side of the y-t diagram. The fork in each line at latter times is the result of a kink wave displacing the specimen away from the barrel. The source of this kink wave is air leaving the gun barrel, providing a lateral displacement to the specimen.

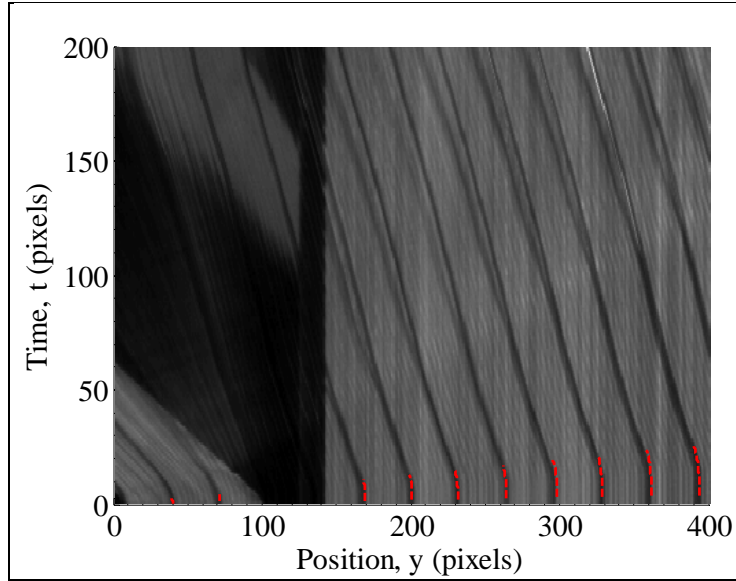


Figure 53. y-t diagram for test 4411o3.

Figure 54 shows the stress-strain relation for test 4411o3 using the power-law model. This dynamic stress-strain relation is stiffer than the quasi-static case and reaches a higher peak stress. This stress-strain relation is not the actual relation experienced during the experiment since localization was not captured in the power-law response.

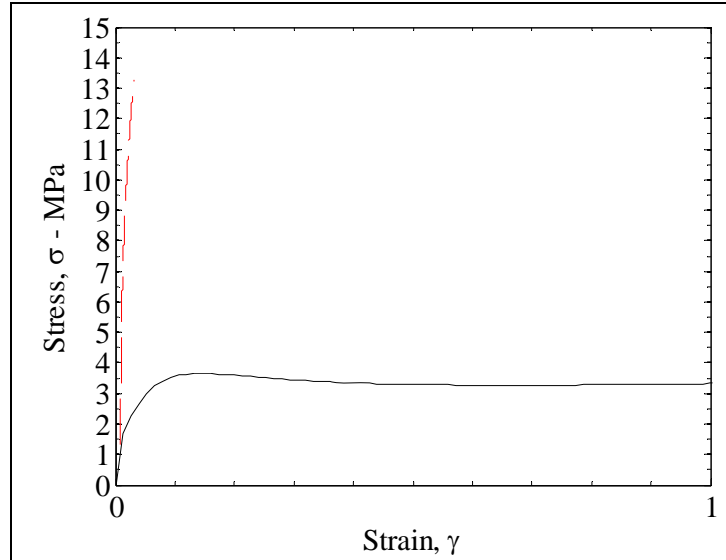


Figure 54. Nominal stress-strain relation for test 4411o3.

Figure 55 shows strain rate as a function of time for test 4411o3. Each black line corresponds to a red dashed line in the y-t diagram. The strain rate is a maximum near the impact end and decreases as the distance down the length of the specimen increases.

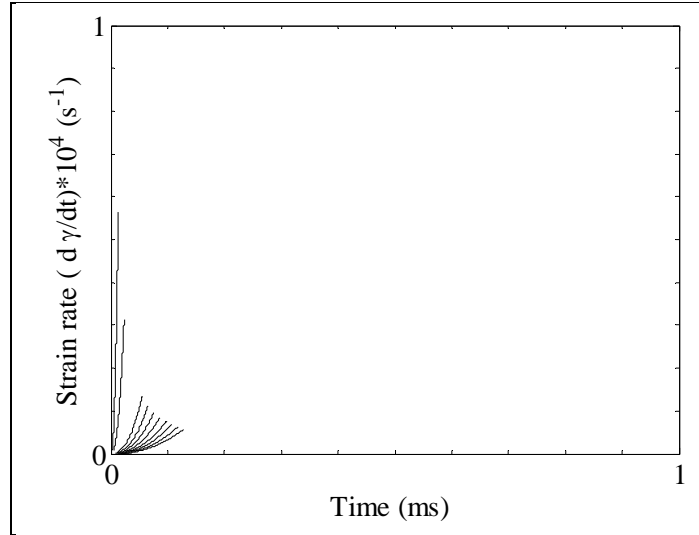


Figure 55. Strain rate as a function of time for test 4411o3.

10.4 Test 4411o4

Figure 56 shows the y-t diagram for test 4411o4. The loading velocity is difficult to measure from the y-t diagram. On top of the y-t diagram are red dashed lines showing particle trajectories obtained from 1-D analysis using the parameters $n = 0.43$ and $\mu = 30$ MPa for the power-law model. The initial strain was $\gamma_0 = 0.019$. The strain at the end of the 1-D analysis was $\gamma_{end} = 0.053$. The largest strain in the y-t diagram was $\gamma_{max} = 1.75$. The fork in each line at 100 pixels is the result of a kink wave displacing the specimen away from the barrel. The source of this kink wave is air leaving the gun barrel, providing a lateral displacement to the specimen. The lateral displacement here is quite significant as the shadow, produced by the light source, displaces initially and then disappears.

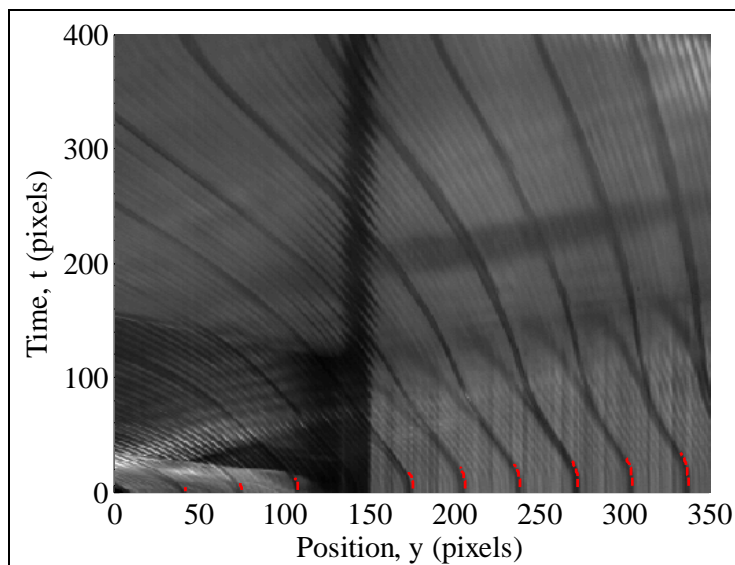


Figure 56. y-t diagram for test 4411o4.

Figure 57 shows the stress-strain relation for test 4411o4 using the power-law model. This dynamic stress-strain relation is stiffer than the quasi-static case and reaches a higher peak stress.

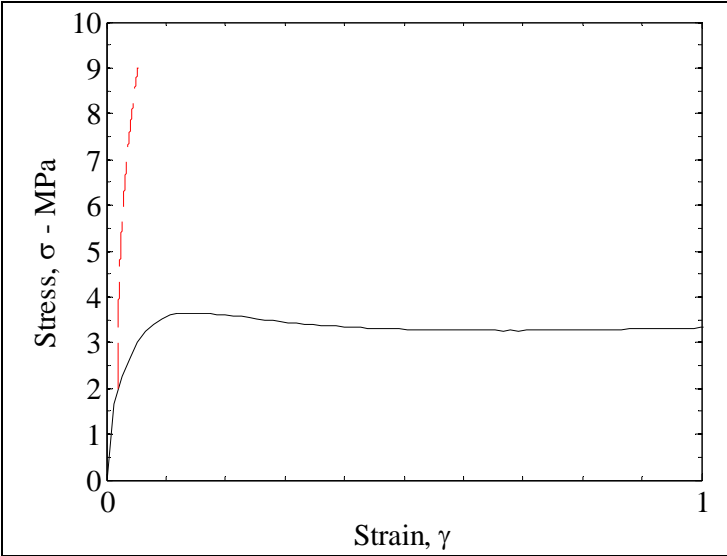


Figure 57. Nominal stress-strain relation for test 4411o4.

Figure 58 shows strain rate as a function of time for test 4411o4. Each black line corresponds to a red dashed line in the y-t diagram. The strain rate is a maximum near the impact end and decreases as the distance down the length of the specimen increases.

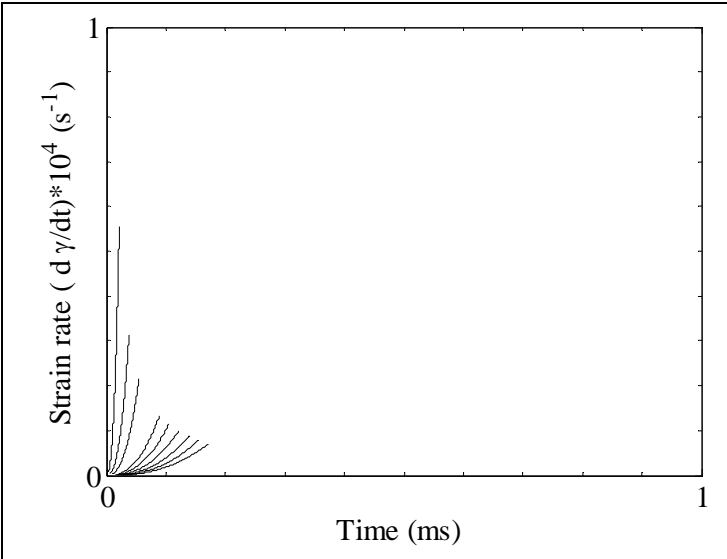


Figure 58. Strain rate as a function of time for test 4411o4.

11. Cross-Section Analysis of 4211o2

Only test 4211o2 was analyzed along the directions perpendicular to the loading direction to determine if this was indeed a uniaxial tensile test for the three sets of parameters in the Swanson model. Figures 59 and 60 show true stress along the half-width and half-thickness, respectively, at $x = 0.029$ m using the full Swanson model. The blue lines correspond to axial true stress, the red lines correspond to the transverse true stress along the width, the green lines correspond to transverse true stress along the thickness, and the black lines correspond to all of the shear stresses. There are 11 lines sampled at equal spacing through the half-width from the center of the specimen to the edge. There are 20 elements across the half-width. There are only two elements through the half-thickness, so there are only two lines for each stress component. We see from these figures that this is uniaxial stress loading since all stresses, except axial true stress, are small in magnitude. We observed similar results for the Swanson model with a reduced number of nonzero parameters.

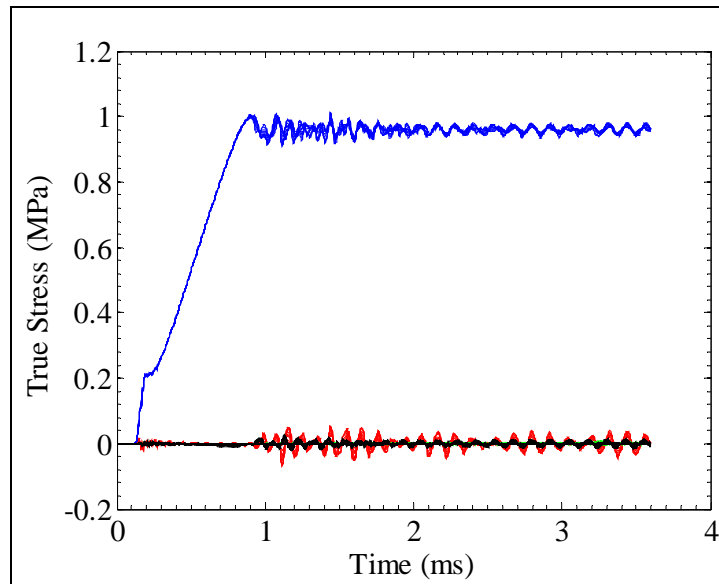


Figure 59. True stress along axis through half-width.

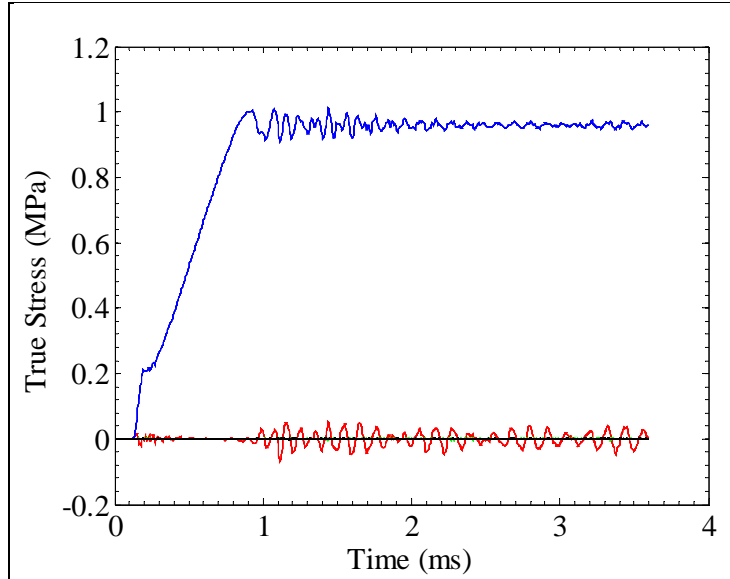


Figure 60. True stress along axis through half-thickness.

Figures 61 and 62 show the log strains along the half-width and half-thickness, respectively, for the full Swanson model. For figure 61, the black line shows the summation of strains along principal axes to show that the volume is nearly incompressible under tensile loading. For figure 62, the black line shows the log shear strains.

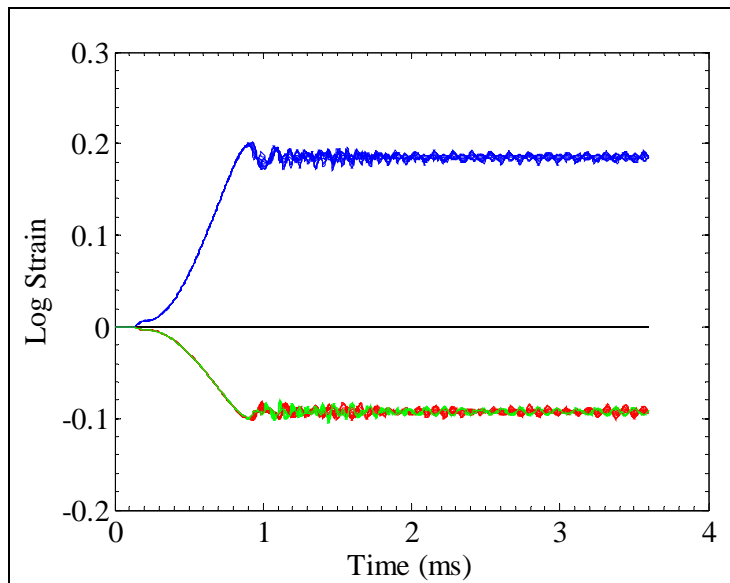


Figure 61. Log strain along axis through half-width.

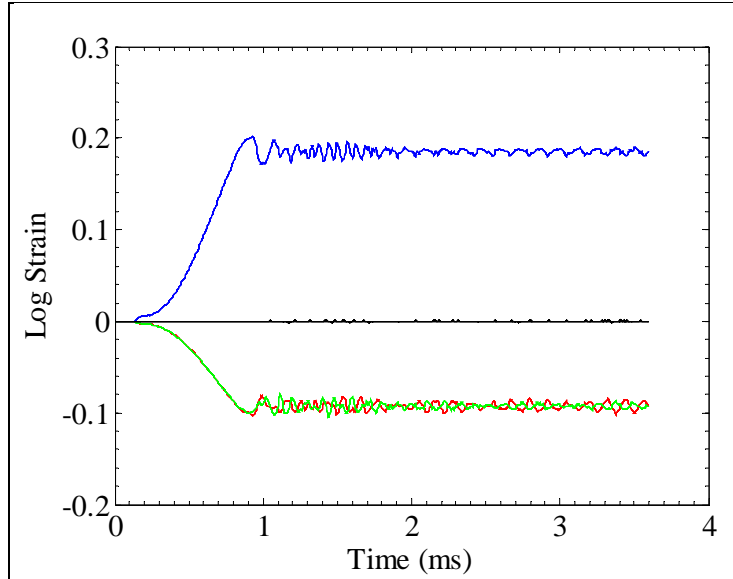


Figure 62. Log strain along axis through half-thickness.

12. Conclusions

The tensile strip stretcher has been confirmed to produce tensile stress waves numerically. Incompressibility has been assumed. A power-law model matches experimental results when the material does not experience localized deformation near the impact end. A Swanson model can then be matched to the power-law model for small strains with one term I_1 or two terms of I_1 and I_2 . To match larger strains, we must add an additional term of I_1 . Small deviations in particle displacement were seen for the Swanson model for some of the experiments, but an optimization procedure for parameters has not been and should not be implemented until additional tests, such as shear and/or compression, have been performed. We did not attempt to actually capture the particle trajectories influenced by the fixed boundary condition in these simulations.

Future research needs to be aimed toward investigating loading from a large prestretch (i.e., $\gamma_0 \neq 0$) since materials of interest may not be in a relaxed state prior to impact. The power-law and Swanson models should continue to hold for vector 4111 and 4211 specimens with an additional term needed to account for initial strain energy (Niemczura and Ravi-Chandar, 2011b). A model accounting for localization is needed to match 4411 specimens. Also, viscoelasticity should be examined to account for relaxation of the material when held at a constant strain prior to impact.

In the future, reflections from the fixed boundary can be examined for purposes of accounting for a larger strain response. For the current conditions implemented, only a small strain response has occurred prior to reflection. Using numerical simulations, we can examine the response of a finite length specimen to dynamic conditions.

13. References

- Niemczura, J.; Ravi-Chandar, K. On the Response of Rubbers at High Strain Rates—I. Simple Waves. *Journal of the Mechanics and Physics of Solids* **2011a**, 59, 423–441.
- Niemczura, J.; Ravi-Chandar, K. On the Response of Rubbers at High Strain Rates—II. Shock Waves. *Journal of the Mechanics and Physics of Solids* **2011b**, 59, 442–456.
- Swanson, S. R. A Constitutive Model for High Elongation Elastic Materials. *Transactions of the ASME* **1985**, 107, 110–114.
- SIERRA Solid Mechanics Team. *Presto 4.16 User's Guide*; Sandia Report 2010-3112; Sandia National Laboratories: Albuquerque, NM, 2010.

NO. OF
COPIES ORGANIZATION

1 DEFENSE TECHNICAL
(PDF INFORMATION CTR
only) DTIC OCA
8725 JOHN J KINGMAN RD
STE 0944
FORT BELVOIR VA 22060-6218

1 DIRECTOR
US ARMY RESEARCH LAB
IMNE ALC HRR
2800 POWDER MILL RD
ADELPHI MD 20783-1197

1 DIRECTOR
US ARMY RESEARCH LAB
RDRL CIO LL
2800 POWDER MILL RD
ADELPHI MD 20783-1197

1 DIRECTOR
US ARMY RESEARCH LAB
RDRL CIO MT
2800 POWDER MILL RD
ADELPHI MD 20783-1197

1 DIRECTOR
US ARMY RESEARCH LAB
RDRL D
2800 POWDER MILL RD
ADELPHI MD 20783-1197

NO. OF
COPIES ORGANIZATION

10 SANDIA NATIONAL LABORATORIES
J NIEMCZURA
MS 0661
PO BOX 5800
ALBUQUERQUE NM 87185

1 US ARMY RSRCH OFC
RDRL ROE M
D STEPP
PO BOX 12211
RESEARCH TRIANGLE PARK
NC 27709-2211

1 US ARMY RSRCH OFC
RDRL ROE V
L RUSSELL
ADELPHI LABORATORY CTR
BLDG 205 R 3A620
ADELPHI MD 20783-1197

2 US ARMY MEDICAL RSRCH &
MATERIEL CMND (USAMRMC)
BLAST INJURY RSRCH PROG
COORDINATING OFC
MCMR RTB
R GUPTA
M LEGGIERI
FT DETRICK MD 21702-5012

2 US ARMY MEDICAL RSRCH &
MATERIEL CMND (USAMRMC)
DIRECTORATE FOR COMBAT
CASUALTY CARE
MCMR RTC
D GIBSON
D HACK
FT DETRICK MD 21702-5012

1 PURDUE UNIV
AERONAUTICS & ASTRONAUTICS
W CHEN
701 W STADIUM AVE
WEST LAFAYETTE IN 47907-2045

2 MASSACHUSETTS INST OF TECHLGY
INST FOR SOLDIER
NANOTECHNOLOGIES
R RADOVITZKY
S SOCRATE
BLDG NE47 4TH FLOOR
CAMBRIDGE MA 02139

NO. OF
COPIES ORGANIZATION

1 UNIV OF FLORIDA
MECHL & AEROSPACE ENGRG
G SUBHASH
GAINESVILLE FL 32611

1 RUTGERS UNIV
DIR OF FED RSRCH RELATIONS
B LAMATTINA
96 FRELINGHUYSEN RD
CORE BLDG
PISCATAWAY NJ 08854

1 HUMAN SYST DEPT
NAVAL AIR WARFARE CTR
AIRCRAFT DIV
B SHENDER
CODE 4656 BLDG 2187 STE 2280A
48110 SHAW RD UNIT 5
PATUXENT RIVER MD 20670-1906

2 DEPT OF MECHL ENGRG
THE JOHNS HOPKINS UNIV
LATROBE 122
V NGUYEN
K T RAMESH
3400 N CHARLES ST
BALTIMORE MD 21218

5 THE JOHNS HOPKINS UNIV APPLD
PHYSICS LAB
T HARRIGAN
A LENNON
A MERKLE
J ROBERTS
M TREXLER
11100 JOHNS HOPKINS RD
LAUREL MD 20723-6099

1 SANDIA NATIONAL LABORATORIES
NANOSCALE & REACTIVE
PROCESSES
S SCHUMACHER
PO BOX 5800 MS 0836
ALBUQUERQUE NM 87185-0836

1 CFD RSRCH CORP
A PRZEK WAS
215 WYNN DR
HUNTSVILLE AL 35805

<u>NO. OF</u> <u>COPIES</u>	<u>ORGANIZATION</u>	<u>NO. OF</u> <u>COPIES</u>	<u>ORGANIZATION</u>
1	UNIV OF NEBRASKA 114G OTHMER HALL N CHANDRA PO BOX 880642 LINCOLN NE 68588-0642	1	BAE SYSTEMS R TANNOUS 9113 LE SAINT DR FAIRFIELD OH 45014-5453
1	UNIV OF TEXAS AUSTIN AEROSPACE ENGRG & ENGRG MECH K RAVI-CHANDAR 1 UNIV STATION C0600 AUSTIN TX 78712-0235	2	SOUTHWEST RSRCH INST MECHL AND MATERIALS ENGRG DIV MATERIALS ENGRG DEPT W FRANCIS D NICOLELLA 6220 CULEBRA RD SAN ANTONIO TX 78238
3	JTAPIC PROGRAM OFC US ARMY MEDICAL RSRCH & MATERIAL CMND MRMC RTB F LEBEDA W LEI J USCILOWICZ 504 SCOTT ST FORT DETRICK MD 21702-5012	1	THE UNIV OF UTAH K L. MONSON 50 S CENTRAL CAMPUS DR 2132 MERRILL ENGRG BLDG SALT LAKE CITY UTAH 84112
1	NAVEL SURFACE WARFARE CTR CODE 664 P DUDT 9500 MACARTHUR DR WEST BETHESDA MD 20817	1	MISSISSIPPI STATE UNIV L WILLIAMS BOX 9632 MISSISSIPPI STATE MS 39762
1	TARDEC RDTA RS R SCHERER BLDG 200C RM 1150 WARREN MI 48397	1	COLUMBIA UNIV B MORRISON 351 ENGINEERING TERRACE 1210 AMSTERDAM AVE MAIL CODE 8904 NEW YORK NY 10027
1	NATICK SOLDIER RSRCH DEV & ENGRG CTR AMSRD NSC WS TB M CARBONI BLDG 4 RM 247 KANSAS ST NATICK MA 01760-5000	1	APPLIED RSRCH ASSOC INC SOUTHWEST DIV C NEEDHAM 4300 SAN MATEO BLVD NE SUITE A-220 ALBUQUERQUE NM 87110
1	AMC NSRDEC M CODEGA KANSAS ST NATICK MA 01760	1	DIR TRAUMATIC INJURY RSRCH PROG DEPT OF MILITARY & EMER MEDICINE UNIFORMED SERVICES UNIV OF THE HEALTH SCIENCES P RAPP 4301 JONES BRIDGE RD BETHESDA MD 20814-4799
1	DEPT OF SURGERY A3020 UNIFORMED SERVICES UNIV A DMITRIEV 4301 JONES BRIDGE RD BETHESDA MD 20814	1	US ARMED FORCES MEDICAL EXAMINER SYST J GETZ 1413 RESEARCH BLVD ROCKVILLE MD 20850

NO. OF
COPIES ORGANIZATION

2 CENTER FOR INJURY
BIOMECHANICS
WAKE FOREST UNIV
F S GAYZIK
J STITZEL
MEDICAL CTR BLVD
WINSTON SALEM NC 27157

1 HENRY JACKSON FOUNDATION
US ARMY AEROMEDICAL RSRCH
LAB
D WISE
6901 ANDREWS AVE
FORT RUCKER AL 36362-0577

1 GARY KAMIMORI
DEPT OF BEHAVIORAL BIOLOGY
WALTER REED ARMY INST OF
RSRCH
503 ROBERT GRANT AVE 2W97
SILVER SPRING MD 20910-7500

ABERDEEN PROVING GROUND

1 US ARMY ABERDEEN TEST CTR
TEDT AT SLB
A FOURNIER
400 COLLERAN RD
ABERDEEN PROVING GROUND MD
21005-5059

79 DIR USARL
RDRL CIH C
P CHUNG
RDRL HRS C
K MCDOWELL
K OIE
B LANCE
W HAIRSTON
RDRL SL
R COATES
RDRL SLB W
W MERMAGEN
M TEGTMEYER
C KENNEDY
P GILLICH
A BREUER
L ROACH
R SPINK
A KULAGA
N EBERIUS
K RAFAELS

NO. OF
COPIES ORGANIZATION

RDRL WML H
M FERREN-COKER
L MAGNESS
B SCHUSTER
RDRL WMM
J ZABINSKI
RDRL WMM B
G GAZONAS
P MOY
RDRL WMM G
C GOLD
B LEIGHLITER
J LENHART
R MROZEK
A RAWLETT
RDRL WMP
P BAKER
S SCHOENFELD
RDRL WMP B
C ADAMS
B LEAVY
R BECKER
S BILYK
J BRADLEY
D CASEM
J CLAYTON
A DAGRO
D DANDEKAR
A DWIVEDI
B EDMANSON
J FITZPATRICK
J GAIR
M GREENFIELD
C A GUNNARSSON
C HOPPEL
J HOUSKAMP
Y HUANG
R KRAFT
B LEAVY
M LYNCH
D MACKENZIE
P J MCKEE
D POWELL
M RAFTENBERG
B SANBORN
S SATAPATHY
M SCHEIDLER (10 COPIES)
T WEERASOORIYA
C WILLIAMS
S WOZNIAK
RDRL WMP C
T W BIERKE
M J GRAHAM
C MEREDITH

NO. OF
COPIES ORGANIZATION

RDRL WMP D
S HALSEY
RDRL WMP E
B LOVE
RDRL WMP F
E FIORAVONTE
A FRYDMAN
N GNIAZDOWSKI
R GUPTA
R KARGUS

NO. OF
COPIES ORGANIZATION

- 1 DSTL BIOMEDICAL SCIENCES
A HEPPER
RM 1A BLDG 245
PORTON DOWN
SALISBURY WILTSHIRE
SP4 OJQ
UNITED KINGDOM
- 4 DRDC VALCARTIER
A BOUAMOUL
L MARTINEAU
D NANDLALL
K WILLIAMS
2459 PIE-XI BLVD. NORTH
QUEBEC QC G3J 1X5 CANADA
- 1 DRDC TORONTO
C BURRELL
1133 SHEPPARD AVE WEST
PO BOX 2000
TORONTO ON M3M 3B9 CANADA
- 1 CIMVHR
A AIKEN
QUEENS UNIV
SCHOOL OF REHABILITATION
THERAPY
KINGSTON ON K7L3N6 CANADA
- 1 HUMAN PROTECTION &
PERFORMANCE DIV
DEFENCE SCIENCE AND TECHLGY
ORGANISATION
DEPT OF DEFENCE
T RADTKE
BLDG 109
506 LORIMER STREET
FISHERMANS BEND VICTORIA 3207
AUSTRALIA

INTENTIONALLY LEFT BLANK.